PAPER • **OPEN ACCESS**

Ray-based inversion accounting for scattering for biomedical ultrasound tomography

To cite this article: Ashkan Javaherian and Ben Cox 2021 *Inverse Problems* **37** 115003

OPEN ACCESS
IOP Publishing
Inverse Problems
Inverse Problems **37** (2021) 115003 (38pp)
https://doi.org/10.1088/1361-6420/ac28ed

Ray-based inversion accounting for scattering for biomedical ultrasound tomography

Ashkan Javaherian* **and Ben Cox**

Department of Medical Physics & Biomedical Engineering, University College London, London WC1E 6BT, United Kingdom

E-mail: a.javaherian@ucl.ac.uk

Received 28 May 2021, revised 6 August 2021
Accepted for publication 21 September 2021
Published 13 October 2021

Abstract

An efficient and accurate image reconstruction algorithm for ultrasound tomography in soft tissue is described and demonstrated, which can recover accurate sound speed distribution from acoustic time series measurements. The approach is based on a second-order iterative minimisation of the difference between the measurements and a model based on a ray-approximation to the heterogeneous Green's function. It overcomes the computational burden of full-wave solvers while avoiding the drawbacks of time-of-flight methods. Through the use of a second-order iterative minimisation scheme, applied stepwise from low to high frequencies, the effects of scattering are incorporated into the inversion.

Keywords: ultrasound tomography, sound speed, ray-based inversion, scattering, Born approximation

(Some figures may appear in colour only in the online journal)

1. Introduction

The aim of ultrasound tomography (UST) is to estimate the acoustic properties of the interior of an object from ultrasonic measurements made on its boundary [6, 9]. There are two related steps: designing and constructing the measurement hardware, and designing and implementing the algorithms to reconstruct the images from the measured data [10]. This paper is concerned with the latter challenge, image reconstruction. Approaches to UST reconstruction

*Author to whom any correspondence should be addressed.

can be classified by (1) the data type used in the inversion, (2) whether the inversion is linearised or nonlinear, (3) the nature of the forward model used. In terms of the data used, there are broadly two categories. The first uses the complete measured time series, including the scattered waves, or its frequency domain components. The second uses only the direct *times-of-flight* between the emitters and receivers; in other words, the data consists just of the time of the first arrival, and no scattered waves are included [8, 11, 12, 27, 38, 39, 59]. The approach we propose here for UST performs a nonlinear inversion by minimising the discrepancy between acoustic pressure time series data and a forward model based on a ray-approximation to the Green's function.

Recently, nonlinear inversion schemes based on a minimisation of the norm of the discrepancy between the measured time series and a full-wave numerical model, which depends on the unknown sound speed, have become popular. Because of the flexibility in the choice of model, this approach—which has become known as *full-wave inversion* [49]—can be very general. When the degree of model-mismatch is low, i.e. when the numerical model accurately represents the measurement scenario, these approaches have the potential to reconstruct accurate, high resolution images. This approach, for which there is a considerable literature in the seismic community [1], has begun to be explored in earnest for medical applications [2, 18, 19, 47, 50–54, 56]. Full-wave approaches are discussed further in section 8, but the biggest challenge with such schemes is the computational cost.

In this paper, we make contributions to both the forward and the inverse problems of UST. We avoid the computational challenge that full-wave models present by using a solver based on a ray-approximation to the Green's function. The ray-based forward model we present is a frequency domain model that can account for refraction by using bent rays, geometric spreading through Green's law, and arbitrary absorption (we use Szabo's model [42–44] but the formulation is general). The principle drawback of using a forward model based on rays is that it inherently neglects scattering. Overcoming this limitation is this paper's principle contribution to tackling the inverse problem. At each step, the Gauss–Newton (GN) search direction is computed by an iterative and implicit computation of the Hessian matrix. Solving the nonlinear inversion in this way implicitly accounts for the primary scattered field (which is sufficient for soft tissue) and can therefore provide high spatial resolution. The non-linearity of the inverse problem and the cycle-skipping problem are handled by first reconstructing a low-contrast sound speed image using a time-of-flight (TOF) approach as an initial guess, and then solving the inverse problem from low to high frequencies [18, 19]. This combination of a ray-based forward model and a second-order inversion scheme provide a computationally efficient method for waveform tomography that avoids the principle drawbacks of both TOF approaches and full-wave solvers.

In section 2, the forward and inverse problems of UST are introduced. In section 3 the forward model—the ray-based approximation to the heterogeneous Green's function—is described. Section 4 explains the second-order approach to the inverse problem, and the calculation of the gradient and Hessian based on the Green's function. The numerical tracing and discretisation of the rays and the Green's functions is described in sections 5 and 6. Numerical examples demonstrating the methods in 2D are given in section 7, although all the results are applicable to 3D. A discussion of the significance of the results and links to similar work follows in section 8.

2. Ultrasonic sound speed tomography

This section describes the forward and inverse problems of sound speed tomography. Let $\boldsymbol{x} = \left(x^1, \ldots, x^d\right)$ denote a spatial position in $\mathbb{R}^d$ with d the dimension. In general, d can be either 2 or

3. This study is restricted to $d = 2$. Accordingly, $\Omega \subset \mathbb{R}^d$ is an open bounded set, and contains the spatially-varying part of the sound speed distribution, $c(\boldsymbol{x})$, i.e. $(c(\boldsymbol{x})/c_0 - 1) \in C_0^\infty$, where c_0 is a scalar value representing the sound speed outside Ω (here the sound speed in water). Also, $\rho(\boldsymbol{x})$ will represent the spatially varying density. The open set Ω is bounded by a circular ring $\mathbb{S} \subset \mathbb{R}$ containing the emission and reception elements.

2.1. Forward problem

2.1.1. Excitation. Sequentially, each emission element, referred to here as emitter $e \in \{1, \ldots N_e\}$, is excited by a pulse and acts as a source $s(t; \boldsymbol{x}_e)$ within the excitation time $t \in (0, T_\mathrm{s})$. The stack-vector of these source time series for all emission elements is denoted by $S \in \mathbb{R}^{(0,T_\mathrm{s})\times N_e}$. Each emitter e is idealised as a point source at $\boldsymbol{x}_e$ with a directional dependence such that the induced acoustic pressure field, $p(t, \boldsymbol{x}; \boldsymbol{x}_e) \in (0, \infty) \times \mathbb{R}^d$, will be a function of $(\boldsymbol{x} - \boldsymbol{x}_e) \cdot \boldsymbol{n}_e$, where $\boldsymbol{n}_e$ is a unit vector giving the orientation of the emitter. (As an example of a practical realisation, each emitter e might be a finite-sized disc centered at $\boldsymbol{x}_e$ with normal $\boldsymbol{n}_e$.)

2.1.2. Measurement. The induced acoustic pressure field is measured at the reception elements, referred to here as receiver $r \in \{1, \ldots, N_r\}$, for times $t \in (0, T)$ with $T \gg T_\mathrm{s}$. For each excitation element e, the time series measured by the receiver r, centered at $\boldsymbol{x}_r$, is represented by $p(t, \boldsymbol{x}_r; \boldsymbol{x}_e)$, where

$$\begin{aligned} \mathcal{M}_{(e,r)} &: (0, \infty) \times \mathbb{R}^d \to \mathbb{R}^{N_\mathrm{t}} \\ p(t, \boldsymbol{x}_r; \boldsymbol{x}_e) &= \mathcal{M}_{(e,r)} \left[p(t, \boldsymbol{x}; \boldsymbol{x}_e) \right], \end{aligned} \tag{1}$$

where N_t is the number of measurement time samples. We have used t here to denote both the continuous and discrete time variables, but the meaning in any particular case should be clear from the context. Furthermore, what is actually measured at $\boldsymbol{x}_r$ is an electrical signal, but we used the same notation p for brevity. As well as acting as a sampling or discretisation operator, $\mathcal{M}_{(e,r)}$ incorporates a filtering stage, corresponding to the frequency-angle dependent response of the receiver. In other words, in general, $\mathcal{M}_{(e,r)}$ not only applies a frequency filter but also depends on $(\boldsymbol{x} - \boldsymbol{x}_r) \cdot \boldsymbol{n}_r$, where $\boldsymbol{n}_r$ is a unit vector giving the orientation of the receiver. (As with the source elements, a practical realisation of a receiver might be a finite-sized disc centered at $\boldsymbol{x}_r$ with normal $\boldsymbol{n}_r$.) While the data is typically measured in the time domain, i.e. with a broadband excitation signal, the image reconstruction will be performed in the frequency domain. To this end, we define the following Fourier transform pair between the time and temporal frequency domains,

$$p(\omega) = \mathscr{F} p(t) = \int_{-\infty}^{\infty} p(t) \mathrm{e}^{\mathrm{i}\omega t} \, \mathrm{d}t, \qquad p(t) = \mathscr{F}^{-1} p(\omega) = \frac{1}{2\pi} \int_{-\infty}^{\infty} p(\omega) \mathrm{e}^{-\mathrm{i}\omega t} \, \mathrm{d}t. \tag{2}$$

Definition 1. Here, the forward operator is defined in the frequency domain.

$$\begin{aligned} \mathcal{A} &: \mathbb{D}(\Omega) \to \mathbb{R}^{N_\omega N_r N_e} \\ P &= \mathcal{A} \left[c(\boldsymbol{x}) \right], \end{aligned} \tag{3}$$

where N_ω is the number of discrete frequencies used. Also, the space $\mathbb{D}$ is defined such that any function $c(\boldsymbol{x}) \in \mathbb{D}$ satisfies $\left(c(\boldsymbol{x})/c_0 - 1\right) \in C_0^\infty(\Omega)$, and $P \in \mathbb{R}^{N_\omega N_r N_s}$ is a stack-vector of measured complex amplitudes with components

$$p_{(c;\omega,r;e)} = \mathcal{A}_{(\omega,r;e)}\,[c]\,, \tag{4}$$

where $\mathcal{A}_{(\omega,r;e)}$ accounts for the selection of the N_ω frequencies, Fourier transformation $\mathscr{F}$, acoustic propagation, and the filtering and sampling described by $\mathcal{M}_{(e,r)}$ in the frequency domain.

2.2. Inverse problem

The inverse problem is now an estimation of the sound speed distribution $c(\boldsymbol{x})$ from the measured data $\hat{p}_{(\omega,r;e)}$, which is the set of recorded complex pressures for all pairs of emission and reception points, given the excitation $s(\omega,\boldsymbol{x}_e) = \mathscr{F}s(t,\boldsymbol{x}_e)$ [49]. (Note that we use the same notations for parameters in time and frequency domains for brevity.) This can be posed as the nonlinear minimisation problem

$$c^* = \underset{c}{\operatorname{argmin}}\,\mathcal{F}(c), \tag{5}$$

where the objective function is in the form

$$\mathcal{F}(c) = \frac{1}{2}\int\left(\sum_{e,r}|\mathcal{A}_{(\omega,r;e)}\,[c] - \hat{p}_{(\omega,r;e)}|^2\right)\mathrm{d}\omega. \tag{6}$$

3. Approximate Green's function for the lossy Helmholtz equation

This section describes how the propagation of acoustic waves are modelled in this study, and introduces the approximate Green's function which is the basis of the inversion method presented in section 4.

3.1. Lossy Helmholtz equation and complex wavevector

A single frequency acoustic pressure field, $p(\omega,\boldsymbol{x})$, in an absorbing medium is often modelled using a lossy Helmholtz equation of the form

$$\left(\tilde{k}(\boldsymbol{x})^2 + \nabla^2\right)p(\omega,\boldsymbol{x};\boldsymbol{x}_e) = -s(\omega,\boldsymbol{x}_e), \quad \tilde{k} = |\tilde{\boldsymbol{k}}|, \tag{7}$$

where $\tilde{\boldsymbol{k}}$ is a complex wavevector that depends on the sound speed $c(\boldsymbol{x})$, the absorption coefficient $\alpha(\boldsymbol{x})$ and the frequency ω. In our case s represents a point source at position $\boldsymbol{x}_e$. By considering a plane wave solution of the form

$$p(\omega,\boldsymbol{x}) \propto \exp(\mathrm{i}(\tilde{\boldsymbol{k}}\cdot\boldsymbol{x} - \omega t)), \tag{8}$$

and writing $\tilde{\boldsymbol{k}} = \boldsymbol{k} + \mathrm{i}\boldsymbol{k}_i$, it is clear that the real part $\boldsymbol{k}$ is related to the phase speed $c_p(\omega)$ of the wave by

$$|\boldsymbol{k}| \equiv k = \omega/c_p(\omega), \tag{9}$$

and the imaginary part is related to the absorption coefficient α by

$$\boldsymbol{k}_i = \alpha(\boldsymbol{k}/k). \tag{10}$$

3.2. Dispersion relation

The wavenumber $\tilde{k}$ and temporal frequency ω are related via a *dispersion relation*, which encapsulates the effects of absorption and dispersion on the wave. In general, then

$$\tilde{k}(\boldsymbol{x}) = \zeta(\omega, c(\boldsymbol{x}), \alpha(\boldsymbol{x})). \tag{11}$$

Many different models of absorption (and the accompanying dispersion) have been proposed for describing the behaviour of soft biological tissue, and each will lead to a different dispersion relation, a different form for the function ζ. As an example, in this subsection we describe the particular absorption model used in the numerical examples in section 7, and the dispersion relation that results from it. However, it is important to note that the methods described in this section, section 3, apart from this one subsection, do not depend on the particular form of the dispersion relation.

3.2.1. Szabo absorption model. A popular model for describing the propagation of acoustic waves in soft tissues is Szabo's absorbing wave equation [43]

$$\left(\frac{1}{c(\boldsymbol{x})^2} \frac{\partial^2}{\partial t^2} - \nabla^2 + \frac{2\alpha_0(\boldsymbol{x})}{c(\boldsymbol{x}) \cos(\pi y/2)} \frac{\partial^{y+1}}{\partial t^{y+1}} \right) p(t, \boldsymbol{x}; \boldsymbol{x}_e) = s(t, \boldsymbol{x}_e), \tag{12}$$

where $\partial^{y+1}/\partial t^{y+1}$ is a fractional time derivative resulting in an absorption coefficient α which follows the frequency power law $\alpha = \alpha_0 \omega^y$. Here, α_0 has units Np(rad s^{-1})$^{-y}$ m^{-1}, and y is the power-law exponent with a non-integer often in the range $1 \leqslant y \leqslant 1.5$ for soft tissue [42, 43]. In the frequency domain, (12) becomes the lossy Helmholtz equation, (7), with complex wavenumber given by [44]

$$\tilde{k} = k + \mathrm{i}\alpha = \frac{\omega}{c} + \alpha \left(\tan(\pi y/2) + \mathrm{i} \right). \tag{13}$$

3.3. Green's functions

In general, the solution of (7) can be written in terms of a Green's function as

$$p(\omega, \boldsymbol{x}) = \int g(\omega, \boldsymbol{x}; \boldsymbol{x}') s(\omega, \boldsymbol{x}') \mathrm{d}\boldsymbol{x}', \tag{14}$$

where the Green's function g satisfies

$$\left(\tilde{k}(\boldsymbol{x})^2 + \nabla^2 \right) g(\omega, \boldsymbol{x}; \boldsymbol{x}') = -\delta(\boldsymbol{x} - \boldsymbol{x}'). \tag{15}$$

As s is a point source, this becomes simply a scaling

$$p(\omega, \boldsymbol{x}; \boldsymbol{x}_e) = g(\omega, \boldsymbol{x}; \boldsymbol{x}_e) s(\omega, \boldsymbol{x}_e). \tag{16}$$

3.3.1. 2D case. In the homogeneous, lossless case the two-dimensional (2D) free-space Green's function is given by [37, 55]

$$g_{0,2\mathrm{D}}(\omega, \boldsymbol{x}; \boldsymbol{x}') = \frac{\mathrm{i}}{4} H_0^{(1)}\left(\phi_0(\boldsymbol{x}; \boldsymbol{x}')\right) \tag{17}$$

$$\approx A_0(\boldsymbol{x}; \boldsymbol{x}') \exp\left(\mathrm{i}(\phi_0(\boldsymbol{x}; \boldsymbol{x}') + \pi/4)\right), \tag{18}$$

where A_0 is an amplitude factor and ϕ_0 is the phase. (The second line gives the large-argument limit approximation, for which the second terms and higher of an associated asymptotic expansion has been neglected, see [55] for further details.) In this lossless, homogeneous case, the phase speed $c_\mathrm{p} = c_0$, the wavenumber $\tilde{k} = k_0 = \omega/c_0$ is real, and the phase is given by

$$\phi_0(\boldsymbol{x}; \boldsymbol{x}') = k_0 |\boldsymbol{x} - \boldsymbol{x}'|. \tag{19}$$

The amplitude is governed purely by geometric spreading (cylindrical spreading):

$$A_0(\boldsymbol{x}; \boldsymbol{x}') = \left(8\pi k_0 |\boldsymbol{x} - \boldsymbol{x}'|\right)^{-1/2} = \left(8\pi \phi_0(\boldsymbol{x}; \boldsymbol{x}')\right)^{-1/2}. \tag{20}$$

In the heterogeneous, absorbing, case we need an approximate form for the Green's function, so we write, by analogy with the homogeneous case:

$$g_{2\mathrm{D}}(\omega, \boldsymbol{x}; \boldsymbol{x}') \approx A(\boldsymbol{x}; \boldsymbol{x}') \exp\left(\mathrm{i}(\phi(\boldsymbol{x}; \boldsymbol{x}') + \pi/4)\right), \tag{21}$$

where the amplitude factor now contains contributions from absorption and refraction as well as geometric spreading. The reader is referred to appendix A.2 for the equivalent formulae for the 3D case. How the phase ϕ and amplitude A are computed in the heterogeneous, absorbing case will be described below in sections 3.4, 5 and 6.

3.4. Ray-based approximation

This section describes, in general terms, how ray theory will be used to compute the terms in the approximate Green's function for heterogeneous absorbing media. (See [3, 4] for a similar approach in the non-absorbing case.) The numerical implementations are described later, in sections 5 and 6.

3.4.1. Dispersive eikonal equation. Substituting the Green's function, (21) or the 3D equivalent, into the lossy Helmholtz equation, and making the assumption, reasonable for soft tissue, that $\alpha^2 \ll k^2$, leads to the following two equations:

$$k^2 A + \nabla^2 A - A \nabla\phi \cdot \nabla\phi = 0, \tag{22}$$

$$2k\alpha A + 2\nabla A \cdot \nabla\phi + A\nabla^2\phi = 0. \tag{23}$$

By making the high frequency approximation $|\nabla^2 A/A| \ll k^2$, the first equation leads to the *dispersive eikonal* equation

$$\nabla\phi \cdot \nabla\phi = k^2. \tag{24}$$

3.4.2. Rays. In this paper, we solve (24) using the concept of rays. Rays are curves that are perpendicular to surfaces of constant phase, i.e. they are tangent to the wavevector $\boldsymbol{k}$, which satisfies

$$\boldsymbol{k} = \nabla\phi, \tag{25}$$

and therefore (24). The following definition of a ray will be useful.

Definition 2. A ray connecting an emission point $\boldsymbol{x}_e$ to an arbitrary point $\boldsymbol{x} \in \Omega$ is defined using $f_{(k,\boldsymbol{x},\boldsymbol{x}_e)}(\boldsymbol{x}') = 0$. A ray is parameterised by the arc length along it, s, by describing it as the line of points $\{\boldsymbol{x}'(s), s \in [0, L_{\text{ray}}]\}$ that satisfy $f_{(k,\boldsymbol{x},\boldsymbol{x}_e)}(\boldsymbol{x}') = 0$, where L_{ray} is the physical arc length of the ray, and $s = 0$ corresponds to the emission point $\boldsymbol{x}_e$. Here, $f_{(k,\boldsymbol{x},\boldsymbol{x}_e)}(\boldsymbol{x}') = 0$ is an implicit representation of the eikonal equation, i.e. the points $\boldsymbol{x}'$ which satisfy $\nabla\phi(\boldsymbol{x};\boldsymbol{x}_e) \cdot \nabla\phi(\boldsymbol{x};\boldsymbol{x}_e) = k^2$, where $\phi(\boldsymbol{x};\boldsymbol{x}_e)$ is the phase at point $\boldsymbol{x}$ with respect to the emission point $\boldsymbol{x}_e$.

The numerical procedure for tracing the rays such that they obey (24) will be described in section 5. Once the rays have been computed, the phase and amplitude of the acoustic field can be calculated along the rays.

3.4.3. Phase along a ray. The phase in the homogeneous, non-dispersive, case is $\phi_0(\boldsymbol{x};\boldsymbol{x}_e) = k_0|\boldsymbol{x} - \boldsymbol{x}_e|$, as we saw above. In the heterogeneous, dispersive case, the phase on a ray can be calculated as the line integral

$$\phi(\boldsymbol{x};\boldsymbol{x}_e) = \int_C \boldsymbol{k} \cdot \mathrm{d}\boldsymbol{x}' + \phi(\boldsymbol{x}_e), \tag{26}$$

$$= \int_\Omega k(\boldsymbol{x}')\delta(f_{(k,\boldsymbol{x},\boldsymbol{x}_e)}(\boldsymbol{x}'))\mathrm{d}\boldsymbol{x}' + \phi(\boldsymbol{x}_e), \tag{27}$$

where the curve C is the ray joining the start point, $\boldsymbol{x}_e$, to the point of interest $\boldsymbol{x}$. The second form arises from the fact that the tangent to curve C is everywhere parallel to $\boldsymbol{k}$.

3.4.4. Absorption along a ray. The amplitude will be written as two factors,

$$A = A_{\text{abs}} A_{\text{geom}}, \tag{28}$$

where the first accounts for amplitude decay due to absorption losses, and the second for geometric spreading and refractive effects. The absorbing factor is the decay along the ray due to absorption. In the homogeneous but absorbing case we have

$$A_{\text{abs}}(\boldsymbol{x};\boldsymbol{x}_e) = \exp\left(-\boldsymbol{k}_i \cdot (\boldsymbol{x} - \boldsymbol{x}_e)\right), \tag{29}$$

which generalises in the case of a non-straight ray to the line integral

$$A_{\text{abs}}(\boldsymbol{x};\boldsymbol{x}_e) = \exp\left(-\int_C \boldsymbol{k}_i \cdot \mathrm{d}\boldsymbol{x}'\right) = \exp\left(-\int_C \alpha\left(\frac{\boldsymbol{k}}{k}\right) \cdot \mathrm{d}\boldsymbol{x}'\right), \tag{30}$$

$$= \exp\left(-\int_\Omega \alpha(\boldsymbol{x}')\delta(f_{(k,\boldsymbol{x},\boldsymbol{x}_e)})\mathrm{d}\boldsymbol{x}'\right). \tag{31}$$

3.4.5. Geometric spreading and refractive losses along a ray. By substituting (28) into (23), with A_{abs} given by (30), gives

$$2k\alpha A_{\text{geom}} + 2\nabla A_{\text{geom}} \cdot \nabla\phi - 2A_{\text{geom}}\frac{\alpha}{k}\boldsymbol{k} \cdot \nabla\phi + A_{\text{geom}}\nabla^2\phi = 0, \tag{32}$$

where we have used $\nabla A_{\text{abs}} = -(\alpha\boldsymbol{k}/k)A_{\text{abs}}$. Using (25), this collapses to

$$\nabla \cdot (A_{\text{geom}}^2 \nabla\phi) = 0. \tag{33}$$

This *transport equation* describes the effect of geometric spreading (including refractive bending) on the amplitude of the wave. From (33), it is possible to derive *Green's law*, which relates the amplitude at two different points along the same ray through knowledge of the ray tube area, S, at those points [63]:

$$A_{\text{geom}}(\boldsymbol{x}) = \left[\frac{(S/\rho c)_{\boldsymbol{x}_{\text{ref}}}}{(S/\rho c)_{\boldsymbol{x}}}\right]^{1/2} A_{\text{geom}}(\boldsymbol{x}_{\text{ref}}). \tag{34}$$

How the reference point $\boldsymbol{x}_{\text{ref}}$ is chosen will be explained below. Section 6, will describe the numerical implementation of the equations in this section.

3.4.6. Reference point. The area of the ray tube at the emission point vanishes [32], so, for a finite pressure source $s(t, \boldsymbol{x}_e)$, if the emission point $\boldsymbol{x}_e$ were chosen as the reference point $\boldsymbol{x}_{\text{ref}}$ then the pressure amplitude calculated using (34) would vanish everywhere. To avoid this, the reference point is chosen to be $\boldsymbol{x}_{\text{ref}} = \boldsymbol{x}_{e'} \in \mathcal{N}(\boldsymbol{x}_e)$ on the ray connecting $\boldsymbol{x}_e$ to $\boldsymbol{x}$, where $\mathcal{N}(\boldsymbol{x}_e)$ is a small neighborhood of the emission point $\boldsymbol{x}_e$ and the distance $|\boldsymbol{x}_{e'} - \boldsymbol{x}_e|$ is a small scalar value. (Here, the reference point is chosen as the first ray point after the emission point.)

Note that $\lim_{\boldsymbol{x}_{e'} \to \boldsymbol{x}_e} S(\boldsymbol{x}_{e'})A_{\text{geom}}(\boldsymbol{x}_{e'})$ is required to be nonzero and bounded and satisfy (34) for a given $A_{\text{geom}}(x)$ in a homogeneous medium [32]. For this to remain true for the heterogeneous case, the acoustic properties inside $\mathcal{N}(\boldsymbol{x}_e)$ are assumed homogeneous. $A(\boldsymbol{x}_{e'})$ is then calculated as the amplitude of the analytic Green's function solution to the wave equation for homogeneous media using (20). Correspondingly, given the source function and the emitter position, (34) can be used to calculate the pressure amplitude at an arbitrary point $\boldsymbol{x}$ under an assumption that the area of the ray tube does not vanish across the medium.

4. Ray-based inversion accounting for scattering

In this section, the approach taken for minimising the objective function (6) in terms of the approximate Green's function introduced in sections 3.3 and 3.4 is explained. The objective function in terms of Green's function in the frequency domain is in the form

$$\mathcal{F}(c) = \frac{1}{2}\int \sum_{e,r} |\delta P_{\text{res}}|^2 \, \mathrm{d}\omega, \tag{35}$$

where δP_{res} is the residual, and has components

$$\delta p_{\text{res}}(c; \omega, r; e) = p_{(c;\omega,r;e)} - \hat{p}_{(\omega,r;e)}, \tag{36}$$

where $p_{(c;\omega,r;e)} = g(c; \omega, \boldsymbol{x}_r; \boldsymbol{x}_e)s(\omega, \boldsymbol{x}_e)$. The minimisation of (35) involves moving to the minimum of an objective function in steps from some starting point $c^{(0)}$. The approach taken in this

study is finding the steps $\delta c^{(n)}$ which minimise the Taylor series approximation [57]

$$\mathcal{F}(c^{(n)}+\delta c^{(n)}) \approx F(c^{(n)}) + \int \frac{\partial \mathcal{F}}{\partial c^{(n)}(\boldsymbol{x}')}\delta c^{(n)}(\boldsymbol{x}')\mathrm{d}\boldsymbol{x}' + O\left((\delta c^{(n)})^2\right), \tag{37}$$

where n is the iteration number, and the second-order terms and higher are truncated. Taking the gradient of (37) with respect to c yields [57]

$$\begin{aligned}\frac{\partial \mathcal{F}\left(c^{(n)}+\delta c^{(n)}\right)}{\partial c^{(n)}(\boldsymbol{x})} &\approx \frac{\partial \mathcal{F}(c^{(n)})}{\partial c^{(n)}(\boldsymbol{x})} + \int \frac{\partial^2 \mathcal{F}(c^{(n)})}{\partial\left(c^{(n)}(\boldsymbol{x})\right)\partial\left(c^{(n)}(\boldsymbol{x}')\right)}\delta c^{(n)}(\boldsymbol{x}')\mathrm{d}\boldsymbol{x}' \\ &= \nabla\mathcal{F}^{(n)}(\boldsymbol{x}) + \int H^{(n)}(\boldsymbol{x},\boldsymbol{x}')\ \delta c^{(n)}(\boldsymbol{x}')\mathrm{d}\boldsymbol{x}',\end{aligned} \tag{38}$$

where the first term on the right-hand side is the gradient of $\mathcal{F}$ at iteration n, and the second term is the action of the Hessian, $H^{(n)}$, on a perturbation $\delta c^{(n)}$. Finding the perturbation that makes this right-hand side zero is equivalent to finding a search direction using a second-order optimisation approach for minimising $\mathcal{F}$. This leads to a linear minimisation sub-problem, which can be solved by matrix-free approaches, and its solution gives a direct step towards the local minimum of the objective function. Taking this approach for minimising the objective function in (35) using the usual good approximation of the Hessian described below is called a GN algorithm, and requires the solution of a *normal equation* for each sub-problem (see section 4.3).

Note that replacing the Hessian with the identity in the above equation will give the steepest descent search direction, which is equivalent to taking a first-order optimisation approach, in which the nonlinear objective function (35) is minimised using a search direction which uses only the information included in the gradient term in (38). First-order approaches [5] are currently in widespread use for full-wave inversion [2, 50–53], because they do not require the additional expense of computing the Hessian. Here, however, the use of a second-order minimisation is the key to incorporating the effects of scattering in the inversion. Unlike with some forward models, this does not impose a significant computational burden, because the Hessian matrix can be efficiently computed using the Greens functions already used for computing the gradient. To understand why the scattering effects are included, note that the pressure $p_{(c;\omega,r;e)}$ modelled using the ray approach described in section 3 above only captures the accumulated information along a ray linking emitter e and receiver r, i.e. the first-arriving signal, and scattering, which allows any point in the medium to contribute to the pressure $p_{(c;\omega,r;e)}$, is neglected. Therefore, using only the information included in the gradient for taking a search direction, scattering effects are neglected. On the other hand, (38) can be expressed as a minimisation sub-problem of the form

$$\delta c^{(n)} \approx \underset{\delta c}{\operatorname{argmin}}\ \frac{1}{2}\int \sum_{e,r} |\delta p_{(c^{(n)};\omega,r;e)}(\delta c) - \delta p_{\mathrm{res}}(c^{(n)};\omega,r;e)|^2\,\mathrm{d}\omega, \tag{39}$$

which seeks to find the search direction $\delta c^{(n)}$ which fits the induced perturbed pressure on the receivers to the residual in a least square sense. The order of dependence of the perturbed pressure $\delta p_{(c^{(n)};\omega,r;e)}$ on δc, which is the same as the order of Taylor series in (37), determines the extent to which scattering is included in (39). Here, the dependence of δP on δc is first order, leading to linear minimisation subproblem, in which δP captures single-scattering (which is usually sufficient for soft biological tissue). Therefore, by solving (35) through a sequence of linear minimisation problems of the form given in (39), scattering can be included in the image reconstruction.

4.1. Fréchet derivative

The Fréchet derivative, $\partial p_{(c^{(n)};\omega,r;e)}/\partial c^{(n)}(\boldsymbol{x})$ indicates the size of the pressure field perturbation δP that will arise from a perturbation in the sound speed δc. The gradient and Hessian can be written in terms of the Fréchet derivative, as will be shown below. The form of the Fréchet derivative of the forward operator (4) will depend on the particular form of the lossy Helmholtz equation used, i.e. it will depend on the form of the dispersion relation, (11). To retain the generality of the derivation, we first find the Fréchet derivative $\partial P/\partial k$ with respect to the wavenumber k. The Fréchet derivative with respect to the sound speed can be found from that straightforwardly using the chain rule:

$$\frac{\partial P}{\partial c} = \frac{\partial P}{\partial k}\frac{\partial k}{\partial c}, \tag{40}$$

where $\partial k/\partial c$ depends on the specific form of the dispersion relation, (11). Recall the lossy Helmholtz equation, (7). A perturbation of $k(\boldsymbol{x})$ at a single point $\boldsymbol{x}'$ by δk will perturb the acoustic field everywhere by $\delta p(\boldsymbol{x})$. Substituting these into (7) gives

$$\left((k+\delta k)^2 - \alpha^2 + 2\mathrm{i}\alpha(k+\delta k) + \nabla^2\right)(p+\delta p) = -s, \tag{41}$$

which, using (7) and neglecting the products of the perturbations, gives

$$\left(k^2 + \nabla^2\right)\delta p(\boldsymbol{x}) = -p\Upsilon\delta k\delta(\boldsymbol{x}-\boldsymbol{x}'), \tag{42}$$

where $\Upsilon = 2(k+\mathrm{i}\alpha)$ and $\Upsilon\delta k$ is a complex scattering potential. The solution of this can be written in terms of the Green's function, (14), so we can write the perturbation of the pressure at any point $\boldsymbol{x}$ as

$$\delta p(\boldsymbol{x};\boldsymbol{x}') = \int g(k,\boldsymbol{x};\boldsymbol{x}'')p(\boldsymbol{x}'')\Upsilon(\boldsymbol{x}'')\delta k\,\delta(\boldsymbol{x}''-\boldsymbol{x}')\mathrm{d}\boldsymbol{x}'', \tag{43}$$

$$= g(k,\boldsymbol{x};\boldsymbol{x}')\Upsilon(\boldsymbol{x}')\delta k(\boldsymbol{x}')g(k,\boldsymbol{x}';\boldsymbol{x}_e)s(\boldsymbol{x}_e), \tag{44}$$

where the latter step used (16). So the Fréchet derivative of the pressure at a point $\boldsymbol{x}$ when emitted from a source at $\boldsymbol{x}_e$ is

$$\frac{\partial p(\boldsymbol{x};\boldsymbol{x}_e)}{\partial k(\boldsymbol{x}')} = g(k,\boldsymbol{x};\boldsymbol{x}')\Upsilon(\boldsymbol{x}')g(k,\boldsymbol{x}';\boldsymbol{x}_e)s(\boldsymbol{x}_e). \tag{45}$$

In particular, the Fréchet derivative of the pressure at the detector position $\boldsymbol{x}_r$ can be computed, for the nth iteration, using

$$\frac{\partial p_{(k^{(n)},r;e)}}{\partial k(\boldsymbol{x}')} = g(k^{(n)},\boldsymbol{x}_r;\boldsymbol{x}')\Upsilon^{(n)}(\boldsymbol{x}')g(k^{(n)},\boldsymbol{x}';\boldsymbol{x}_e)s(\boldsymbol{x}_e). \tag{46}$$

This has a clear interpretation, reading from right to left: the source s at point $\boldsymbol{x}_e$ is propagated to the point $\boldsymbol{x}'$ in the domain by the Green's function $g(\boldsymbol{x}';\boldsymbol{x}_e)$, whereupon it is multiplied by Υ and propagated to the receiver point $\boldsymbol{x}_r$ by the Green's function $g(\boldsymbol{x}_r;\boldsymbol{x}')$.

4.1.1. Szabo absorption model. In order to obtain the Fréchet derivative with respect to the sound speed c, rather than k, we need to use a dispersion relation linking these quantities, i.e. we need to decide on a particular absorption model. In section 3.2.1, a form of the dispersion relation for Szabo's absorption model was introduced in (13):

$$k = \frac{\omega}{c} + \alpha\,\tan(\pi y/2), \tag{47}$$

so

$$\begin{aligned}\frac{\partial p}{\partial c} &= \frac{\partial p}{\partial k}\frac{\partial k}{\partial c} = -\frac{\omega}{c^2}\frac{\partial p}{\partial k},\\ \frac{\partial p_{(c^{(n)};r;e)}}{\partial c(\boldsymbol{x})} &= g(c^{(n)};\boldsymbol{x}_r;\boldsymbol{x})\Upsilon_c^{(n)}(\boldsymbol{x})g(c^{(n)};\boldsymbol{x};\boldsymbol{x}_e)s(\boldsymbol{x}_e),\end{aligned} \tag{48}$$

where

$$\Upsilon_c^{(n)}(\boldsymbol{x}) = \frac{-2\omega}{c(\boldsymbol{x})^2}\left(\frac{\omega}{c(\boldsymbol{x})} + \alpha(\boldsymbol{x})(\tan(\pi y/2) + \mathrm{i})\right). \tag{49}$$

4.2. Gradient and Hessian

The gradient can be written as the action of the Fréchet derivative on the conjugate of the residual $\delta P^*_{\mathrm{res}}$ as

$$\nabla\mathcal{F}^{(n)}(\boldsymbol{x}) = \sum_{e,r}\int \mathrm{Re}\left\{\frac{\partial p_{(c^{(n)};r;e)}}{\partial c^{(n)}(\boldsymbol{x})}\delta p^*_{\mathrm{res}}(c^{(n)};r;e)\right\}\mathrm{d}\omega, \tag{50}$$

$$\begin{aligned}&= \sum_{e,r}\int \mathrm{Re}\left\{\Upsilon_c^{(n)}(\boldsymbol{x})\left[g(c^{(n)};\boldsymbol{x};\boldsymbol{x}_e)s(\boldsymbol{x}_e)\right]\right.\\ &\quad\times\left.\left[g(c^{(n)};\boldsymbol{x}_r;\boldsymbol{x})\ \delta p^*_{\mathrm{res}}(c^{(n)};r,e)\right]\right\}\mathrm{d}\omega,\end{aligned} \tag{51}$$

where we have used (48). Similarly, the action of the Fréchet derivative on the perturbation δP gives a commonly used, and very good, approximation to the action of the Hessian on the sound speed perturbation:

$$(H^{(n)}\delta c^{(n)})(\boldsymbol{x}) \approx \sum_{e,r}\int \mathrm{Re}\left\{\frac{\partial p_{(c^{(n)};r;e)}}{\partial c^{(n)}(\boldsymbol{x})}\delta p^*_{(c^{(n)};r;e)}\right\}\mathrm{d}\omega, \tag{52}$$

$$\begin{aligned}&= \sum_{e,r}\int \mathrm{Re}\left\{\Upsilon_c^{(n)}(\boldsymbol{x})\left[g(c^{(n)};\boldsymbol{x};\boldsymbol{x}_e)s(\boldsymbol{x}_e)\right]\right.\\ &\quad\times\left.\left[g(c^{(n)};\boldsymbol{x}_r;\boldsymbol{x})\ \delta p^*_{(c^{(n)};r;e)}\right]\right\}\mathrm{d}\omega,\end{aligned} \tag{53}$$

where again we have used (48). In both of these integrals, all the factors of the integrand depend on frequency ω. The square brackets here and above just indicate a way of interpreting this formulation of the gradient as the product of a forward propagation of the source by the Green's function, and backwards propagating of the residual by its adjoint. In other words, in (48), $g(\boldsymbol{x}_r;\boldsymbol{x})$ acts as a forward propagator from $\boldsymbol{x}$ to $\boldsymbol{x}_r$, whereas in equations (51) and (53), it acts as a backward propagator from $\boldsymbol{x}_r$ to $\boldsymbol{x}$. Note that the Green's function obeys the reciprocity relation $g(\boldsymbol{x};\boldsymbol{x}') = g(\boldsymbol{x}';\boldsymbol{x})$.

We emphasise here again the reason for using the Hessian in the inversion. The residual, δp_{res}, which appears in the expression for the gradient, (51), depends only on the points along a ray linking e and r, and therefore it includes only refractive effects. However, the pressure perturbation δp which appears in the expression for the Hessian, (53), can be affected by any

point in the medium, because it is obtained from the action of the Frećhet derivative, on the sound speed perturbation, δc, which can vary anywhere. Therefore, solving the minimisation subproblem (39), which gives the normal equation (38), can account for single scattering in a way that the ray-based gradient cannot. This is the reason why, when using a ray-based forward model, a GN approach to the inversion step, rather than a purely gradient-based approach, is critical for obtaining good reconstructions.

4.3. Normal equation and update computation

Having defined the gradient and Hessian, this section explains how they are included in (38) and a GN step direction is calculated. In this case, the linear subproblem, (38), takes the form of the normal equation, which is solved using a *conjugate gradient* (CG) algorithm. The procedure is outlined below.

In algorithm 1, l is the number of cg iterations, and the CG algorithm is terminated after a fixed $l_{\max}$ number of iterations. The sound speed is then updated using a step length τ, which is fixed for all linear subproblems n. Also, the Green's functions included in $\nabla\mathcal{F}^{(n)}$ and $H^{(n)}$ are dependent on the chosen angular frequencies ω. Algorithm 1 is iteratively implemented by choosing a range including small frequencies for $c^{(0)}$, and increasing the frequency range for the next linearised subproblems.

5. Numerical ray tracing

This section, and the following section, describe the numerical implementation of the method described above for implementing UST. It is therefore worth taking stock at this point and recapping the essential principles. We aim to reconstruct an image of the sound speed by minimising the objective function $\mathcal{F}$ in (35) through an iterative formation of the linear subproblem (38), and solving it by means of a CG algorithm given in algorithm 1. The first term in (38) is the functional gradient $\nabla\mathcal{F}$, and is calculated using (51). The second term is an action of the Hessian matrix on a perturbation to the sound speed, and is calculated using (53) and (43). These formulae are functions of the Green's functions $g(c^{(n)};\omega,\boldsymbol{x};\boldsymbol{x}_e)$ and $g(c^{(n)};\omega,\boldsymbol{x}_r;\boldsymbol{x})$. The phase in the Green's function is computed from equation (26), and the amplitude A is computed from equations (30) and (34). All these formulae rely on the rays introduced in section 3.4.2. How those rays are traced in practice is described in this section.

5.1. Ray equations

In section 3.4, as a means of solving the dispersive eikonal equation (24), rays with direction vector $\boldsymbol{k}(\boldsymbol{x}) = \nabla\phi(\boldsymbol{x})$ were introduced. It can be straightforwardly shown that the unit vector $\mathrm{d}\boldsymbol{x}/\mathrm{d}s$, describing how the position vector $\boldsymbol{x}(s)$ changes with distance along the ray s, and the wavevector $\boldsymbol{k}$ must satisfy the coupled *ray equations*

$$\frac{\mathrm{d}\boldsymbol{x}}{\mathrm{d}s} = \frac{\boldsymbol{k}}{k}, \qquad \frac{\mathrm{d}\boldsymbol{k}}{\mathrm{d}s} = \nabla k. \tag{54}$$

In UST, the rays must always start at an emission point $\boldsymbol{x}_e$ and end at a receiver point $\boldsymbol{x}_r$. Computing rays to link two points like this is known as *two-point* ray tracing [25]. In this context it is instructive to consider Fermat's principle [34, 63], which states that the path between two points taken by a ray makes the acoustic length stationary under variations in a family of nearby paths.

The trajectory of a ray passing from point p_1 to p_2 can be interpreted in the Lagrangian sense in different ways. Here, following [34], the trajectories of rays are chosen as the stationary

Algorithm 1. CG algorithm for computing update.

input: $c^{(n)},\ \mathcal{F}(c^{(n)}), l_{\max}$
initialise: $l = 0,\ \delta c_l^{(n)} = 0$
$r_l \leftarrow \nabla \mathcal{F}^{(n)}$ using (51) ▷ Initialise the cg (inner) residual
$d_l = r_l$ ▷ Initialise the cg (inner) step direction
while $l < l_{\max}$ **do** ▷ Iterate for a fixed number of iterations
  $z_l \leftarrow H^{(n)} d_l$ ▷ Update the action of the Hessian on the cg step direction using (52)
  $\alpha_l \leftarrow \frac{r_l^{\mathrm{T}} r_l}{d_l^{\mathrm{T}} z_l}$ ▷ Update the cg step size 1
  $\delta c_{l+1}^{(n)} \leftarrow \delta c_l^{(n)} + \alpha_l d_l$ ▷ Update the sound speed perturbation
  $r_{l+1} \leftarrow r_l - \alpha_l z_l$ ▷ Update the cg residual
  $\beta_l \leftarrow \frac{r_{l+1}^{\mathrm{T}} r_{l+1}}{r_l^{\mathrm{T}} r_l}$ ▷ Update the cg step size 2
  $d_{l+1} \leftarrow r_{l+1} + \beta_l d_l$ ▷ Update the step direction
  $l \leftarrow l + 1$ ▷ Increment the counter
end while
output: $c^{(n+1)} \leftarrow c^{(n)} + \tau \delta c_*^{(n)}$ ▷ Return the optimal sound speed

points of an 'action' given by

$$\int_{p_1}^{p_2} \mathcal{L}\,\mathrm{d}s, \quad \mathcal{L}(\dot{\boldsymbol{x}}, \boldsymbol{x}, s) = k(\boldsymbol{x})\,(\dot{\boldsymbol{x}} \cdot \dot{\boldsymbol{x}})^{1/2}, \tag{55}$$

where $\dot{\boldsymbol{x}} \equiv \mathrm{d}\boldsymbol{x}/\mathrm{d}s$. Also, $\mathrm{d}s = |\mathrm{d}\boldsymbol{x}(s)|$ is an infinite simal distance along the ray, and thus $|\dot{\boldsymbol{x}}| = 1$. The generalised momentum variables are defined as

$$\kappa_i = \partial\mathcal{L}/\partial\dot{x}_i = k\dot{\boldsymbol{x}}, \tag{56}$$

which satisfies the left equation in (54). The action is minimised by the Euler–Lagrange equation

$$\frac{\mathrm{d}}{\mathrm{d}s}\frac{\partial\mathcal{L}}{\partial\dot{\boldsymbol{x}}} = \frac{\partial\mathcal{L}}{\partial\boldsymbol{x}}, \tag{57}$$

which directly leads to the right equation in (54).

Interestingly, many different Hamiltonian systems can be defined whose bicharacteristic curves can be associated with the rays as defined here [3, 22–24, 32, 41].[1] In practice, equation (54) are solved using a numerical ray-tracing algorithm combined with *ray-linking* techniques, as described below.

5.2. Ray tracing with Heun's method

Several algorithms for computing rays that satisfy equation (54) are described in the literature, see e.g. [14, 24–26, 28, 32, 41]. In reference [31], section 2.2, a short comparison has been provided between ray tracing algorithms. An implementation of the ray equations derived in (54) using a second-order variant of Runge–Kutta (RK) scheme provides a good trade-off between accuracy and speed [29, 33]. Therefore, this approach has been taken in this study.

Consider a ray, and for a point m along the ray let us define $y_m = [\boldsymbol{x}_m, \boldsymbol{\kappa}_m]^{\mathrm{T}} \in \mathbb{R}^{2d}$. Using a second-order variant of RK method, also known as *improved Euler* or *Heun's* method, y_{m+1} can be approximated in the form

$$y_{m+1} = y_m + \frac{\Delta s}{2}(q(y_m) + q(\hat{y}_{m+1})), \tag{58}$$

where

$$q(y) = \begin{bmatrix} q_{\boldsymbol{x}} \\ q_{\boldsymbol{\kappa}} \end{bmatrix} = \begin{bmatrix} \boldsymbol{\kappa}/k(\boldsymbol{x}) \\ \nabla k(\boldsymbol{x}) \end{bmatrix}, \tag{59}$$

and

$$\hat{y}_{m+1} = y_m + \Delta s\, q(y_m). \tag{60}$$

Each step m involves first calculating an auxiliary variable $\hat{y}_{m+1}$, which is a predictor for the next update, and then correcting the update y_{m+1} through (58) using a trapezoid rule. Therefore,

[1] Equivalently, rays can be expressed as the characteristic curve of the Hamiltonian $H(\boldsymbol{x}, \boldsymbol{\kappa})$, which can also be defined in different ways. For example, $H(\boldsymbol{x}, \boldsymbol{\kappa}) = \boldsymbol{\kappa} \cdot \boldsymbol{\kappa}/(2k^2)$ $(H = 1/2)$ [23], $H(\boldsymbol{x}, \boldsymbol{\kappa}) = (\boldsymbol{\kappa}^2 - k^2)/2$ $(H = 0)$ [30], or $H(\boldsymbol{x}, \boldsymbol{\kappa}) = |\boldsymbol{\kappa}|/k(H = 1)$ [24]. All these Hamiltonian formulae satisfy the eikonal equation (24) [41]. The characteristic curves of these Hamiltonian systems satisfy $\mathrm{d}\boldsymbol{x}/\mathrm{d}s = \nabla_{\boldsymbol{\kappa}} H(\boldsymbol{x}, \boldsymbol{\kappa})$ and $\mathrm{d}\boldsymbol{\kappa}/\mathrm{d}s = -\nabla_{\boldsymbol{x}} H(\boldsymbol{x}, \boldsymbol{\kappa})$, which together with imposing the condition $|\mathrm{d}\boldsymbol{x}/\mathrm{d}s| = 1$, give the ray equation (54).

Algorithm 2. Ray tracing using Heun's method.

input: $\boldsymbol{x}_e$, $k \coloneqq k(\boldsymbol{x})$ ▷ Input initial ray position and wavenumber
initialise: $\boldsymbol{x} = \boldsymbol{x}_{\bar{e}}$, $\boldsymbol{\kappa} = \boldsymbol{\kappa}_{\bar{e}}$ ▷ Set initial ray position and direction
while $\boldsymbol{x}(s)$ is inside Ω **do**
  $\boldsymbol{\kappa} \leftarrow k\boldsymbol{\kappa}/|\boldsymbol{\kappa}|$ ▷ Normalise the ray direction
  $q_{\boldsymbol{x}} = \boldsymbol{\kappa}/k$ ▷ Compute the update variables using (59)
  $q_{\boldsymbol{\kappa}} = \nabla k(\boldsymbol{x})$
  $\boldsymbol{\kappa}' \leftarrow \boldsymbol{\kappa} + \Delta s q_{\boldsymbol{\kappa}}$ ▷ Update the auxiliary ray direction
  $k' \leftarrow k(\boldsymbol{x} + \Delta s q_{\boldsymbol{x}})$ ▷ Update the auxiliary wavenumber
  $\boldsymbol{\kappa}' \leftarrow k'\boldsymbol{\kappa}'/|\boldsymbol{\kappa}'|$ ▷ Normalise the auxiliary ray direction
  $q'_{\boldsymbol{x}} = \boldsymbol{\kappa}'/k'$ ▷ Compute the auxiliary update variables using (59)
  $q'_{\boldsymbol{\kappa}} = \nabla k(\boldsymbol{x} + \Delta s q_{\boldsymbol{x}})$
  $\boldsymbol{x} \leftarrow \boldsymbol{x} + (\Delta s/2)(q_{\boldsymbol{x}} + q'_{\boldsymbol{x}})$ ▷ Update the ray position using (58)
  $\boldsymbol{\kappa} \leftarrow \boldsymbol{\kappa} + (\Delta s/2)(q_{\boldsymbol{\kappa}} + q'_{\boldsymbol{\kappa}})$ ▷ Update the ray direction using (58)
end while

the improved Euler method is a predictor–corrector method [29]. In addition, the step directions are normalised such that $|\boldsymbol{\kappa}| = k$, which ensures $\dot{\boldsymbol{x}} \cdot \dot{\boldsymbol{x}} = 1$. The ray tracing algorithm using Heun's method is outlined in algorithm 2.

5.3. Grid-to-ray interpolation

The wavenumber field $k(\boldsymbol{x})$ was represented on a discretised mesh of N_n points x_i. A rectilinear grid was used with grid points indexed with the multi-index $i = (i^1, i^2) \in \{1, \ldots, N_n^1\} \times \{1, \ldots, N_n^2\}$ with $N_n = \prod_{j=1}^{2} N_n^j$ and an equal grid spacing Δx along all Cartesian coordinates j. (Recall that our study is restricted to $d = 2$.) Also, x_{ij} is used to indicate the position of grid point i along Cartesian coordinate j. The points along a ray can lie on any arbitrary points in Ω, and are not restricted to the grid points. Therefore, an interpolation from the grid to the rays must be performed to find the approximate values for k and ∇k used in the ray tracing algorithms [25, 31]. Here, the wavenumber function $k(\boldsymbol{x})$ is represented with a set of B-spline functions, which therefore gives continuous values for the directional gradients. Following [30, 31], the control points for the B-spline function are chosen on the grid points $Q(x_{i^1}, x_{i^2})$, and the B-spline function is defined using

$$k(\boldsymbol{x}) \approx \hat{k}(\boldsymbol{x}) = \sum_{q^1=0}^{3} \sum_{q^2=0}^{3} Y_{q^1}(u) Y_{q^2}(v) Q(x_{i^1+q^1-1}, x_{i^2+q^2-1}). \tag{61}$$

Here, u and v are defined as

$$u(\boldsymbol{x}) = \begin{cases} \dfrac{x^1 - x_{i^1}}{\Delta x}, & \text{if } x_{(i-1)^1} < x^1 < x_{(i+1)^1} \\ 0, & \text{otherwise} \end{cases}$$
$$v(\boldsymbol{x}) = \begin{cases} \dfrac{x^2 - x_{i^2}}{\Delta x}, & \text{if } x_{(i-1)^2} < x^2 < x_{(i+1)^2} \\ 0, & \text{otherwise,} \end{cases} \tag{62}$$

where $x_{(i\pm1)^j}$ denotes the two grid points adjacent to the grid point $x_i = (x_{i^1}, x_{i^2})$ along the Cartesian coordinate j. Here, the polynomials $Y_m(u)$ and $Y_n(v)$ satisfy [31]

$$\begin{bmatrix} Y_0(u) \\ Y_1(u) \\ Y_2(u) \\ Y_3(u) \end{bmatrix} = \frac{1}{6} \begin{bmatrix} -1 & 3 & -3 & 1 \\ 3 & -6 & 0 & 4 \\ -3 & 3 & 3 & 1 \\ 1 & 0 & 0 & 0 \end{bmatrix} \begin{bmatrix} u^3 \\ u^2 \\ u \\ 1 \end{bmatrix}. \tag{63}$$

Using equations (61) and (63), the approximated wavenumber field is $\mathcal{C}^2$ continuous [30, 31]. Therefore, the components of the directional gradients can be analytically calculated from (63).

5.4. Ray-linking

The rays initialised from an emitter at point $\boldsymbol{x}_e$ are used for two tasks, (1) computing the Green's function at the reception points $\boldsymbol{x}_r$, i.e. $g(c^{(n)}; \omega, \boldsymbol{x}_r; \boldsymbol{x}_e)$, which is used for calculating the residual δP_{res}, and (2) computing the Green's function at arbitrary points within the medium $\boldsymbol{x}$ from excitation e, i.e. $g(c^{(n)}; \omega, \boldsymbol{x}; \boldsymbol{x}_e)$. Tracing individual rays from $\boldsymbol{x}_e$ to every point in the domain separately would be much too expensive and many of the rays would be redundant. There are therefore two choices: (a) send rays from $\boldsymbol{x}_e$ at evenly-spaced initial angles out across the whole domain with no specific end-point in mind, and interpolate from these rays onto $\boldsymbol{x}$ and $\boldsymbol{x}_r$ as required, or (b) trace rays from $\boldsymbol{x}_e$ to $\boldsymbol{x}_r$ using ray-linking and then, using those rays, interpolate onto the points $\boldsymbol{x}$ as required. The downsides of option (a) are that there will be interpolation error in the estimate of the pressure at the reception point $\boldsymbol{x}_r$. Therefore, the spacing for the initial angles should be sufficiently small. More importantly, the acoustic length between two points on such a ray is less likely to be a global minimum [25]. With option (b), on the other hand, ray-linking seeks to find a ray trajectory which provides the stationary point within a family of neighborhood paths between $\boldsymbol{x}_e$ and $\boldsymbol{x}_r$ by enforcing a boundary condition on the rays' path such that the ray initialised from an emitter e is intercepted by the receiver r after travelling across the medium. For each iteration (linear subproblem) of the UST inverse problem, and emitter–receiver pair, ray linking is done by iteratively adjusting the initial angle of the ray emanated from the emitter using an optimisation algorithm such that the interception point of the ray by the detection surface matches the position of the receiver within a tolerance. (See [25, 27, 40] for further details.) The main downside of (b) is that *per ray* it is more expensive than (a) because the ray-linking is iterative. However, there are several advantages to using ray-linking. First, because of the imposition of the boundary condition on the ray, the approach is more stable in the following sense: the trajectory of the ray for option (a) doesn't link e to r but to a point different from r, and the phase and amplitude difference between this point and r may be too large to correct using a simple interpolation, resulting in errors in the phase and amplitude. Second, the linked rays can be re-used when calculating the adjoint field, as they link directly to the receiver points from which the adjoint sources emanate.

The most popular ray-linking approaches for 2D media are based on solving the associated one-dimensional inverse problem using the *regula falsi* or *secant* approaches [25, 26, 32, 40, 41]. The *regula falsi* approach will be used for validation of the ray tracing using a digital breast phantom, and a *secant* approach will be used iteratively for solving the optimisation problem in a way in which the linked rays used for solving the linearised problem n will be used as an initial guess for the ray linking for the next subproblem $n + 1$. (See [27] for an extension of ray-linking to 3D.)

5.5. Ray coordinates

In the general case, the coordinates of the ray are given by two parameters: one specifying the initial direction of the ray and another monotonic parameter along the ray [32]. These parameters can be chosen in different ways. For our 2D case, the ray coordinates will be defined as the initial direction of the ray in polar coordinates, which is also called *radiation angle*, and the arc length s along the ray, with $s = s_0$ matching the emission point, and monotonically growing along the ray.

Definition 3. The trajectory of a ray linking an emission point e to a reception point r is defined by the points with arc lengths $s_m,\ m \in \{0, \ldots, M_{(e,r)}\}$, where the number of the sampled points along the ray is $M_{(e,r)} + 1$. Therefore, the points are initialised from s_0 with $\boldsymbol{x}(s_0) := \boldsymbol{x}_e$, and are terminated at the point $s_{M_{(e,r)}}$ with $\boldsymbol{x}(s_{M_{(e,r)}}) := \boldsymbol{x}_r$, the position of receiver r. The points s_m satisfy

$$s_m = \begin{cases} m\Delta s, & m \in \{0, \ldots, M_{(e,r)} - 1\} \\ (m-1)\,\Delta s + \Delta s', & m = M_{(e,r)}. \end{cases} \tag{64}$$

Here, the second line is used in order to indicate that the last point of the ray must be matched to the reception point r, and thus $\Delta s' = s_{M_{(e,r)}} - s_{M_{(e,r)-1}}$ with $\Delta s' \leqslant \Delta s$ [27].

Definition 4. For each excitation e, the pressure field is approximated on a set of linked rays $f_{(k,\boldsymbol{x}_r;\boldsymbol{x}_e)} = 0,\ e \in \{1, \ldots, N_e\},\ r \in \{1, \ldots, N_r\}$. These rays are parameterised in space using $\boldsymbol{x}(s_m, \theta_{(r,e)})$, which denotes the position on the arc length s of the point m along a ray linking the emission position $\boldsymbol{x}_e$ to the reception position $\boldsymbol{x}_r$. Also, the polar initial direction of this ray is indicated by $\theta_{(r,e)}$.

Having defined the rays linking all emitter–receiver pairs, the sampled points along these rays are used for a spatial parameterisation of the medium and for a numerical implementation of the method approximating the acoustic field as described in section 3. The discretised version of this theory is the topic of the next section.

6. Discretisation of approximate Green's function

This section describes how the model outlined in section 3 is discretised for implementation. The Green's function, $g(\omega, \boldsymbol{x}; \boldsymbol{x}_e)$, is discretised at the sampled points along the rays linking the emitter e to all receivers r using the coordinates defined in definition 4

$$\begin{aligned} &g\left(\omega; \boldsymbol{x}(s_m, \theta_{(r,e)})\right) \\ &\quad \approx A\left(\boldsymbol{x}(s_m; \theta_{(r,e)}\right) \exp\left(\mathrm{i}\left(\phi\left(\boldsymbol{x}(s_m, \theta_{(r,e)})\right) + \pi/4\right)\right), \end{aligned} \tag{65}$$

where $\phi\left(\boldsymbol{x}(s_m, \theta_{(r,e)})\right)$ and $A\left(\boldsymbol{x}(s_m, \theta_{(r,e)})\right)$ are the phase and amplitude on point m on the ray linking emitter e to receiver r, respectively.

6.1. Acoustic absorption

The acoustic absorption on the ray is computed in the form

$$A_{\mathrm{abs}}\left(\boldsymbol{x}(s_m, \theta_{(r,e)})\right) = \exp\left(-\int_{s_0}^{s_m} \alpha\left(\boldsymbol{x}(s_m, \theta_{(r,e)})\right) \mathrm{d}s\right), \tag{66}$$

where $A_{\mathrm{abs}}\left(\boldsymbol{x}(s_0, \theta_{(r,e)})\right) = 1$.

6.2. Geometrical spreading

The effect of geometric spreading on the amplitude of Green's function is described in (34), which relates the amplitudes at two points along a ray by considering how the area of the *ray tube* around the ray changes between the two points, as described in section 3.4.5. To compute this numerically requires us to estimate the rate at which two closely-spaced rays diverge, for which we turn to the concept of the *ray Jacobian* [32].

First, note that the relations between the ray coordinates, $\gamma = [\gamma_1, \gamma_2]^{\mathrm{T}} = \left[\theta_{(r,e)}, s_m\right]^{\mathrm{T}}$ and the general Cartesian coordinates, $\boldsymbol{x} = [x_1, x_2]^{\mathrm{T}}$, follows

$$Q_{ii'}(s_m, \theta_{(r,e)}) = \frac{\partial x_i}{\partial \gamma_{i'}}(s_m, \theta_{(r,e)}), \tag{67}$$

where Q is called the *transformation matrix*, and satisfies

$$\mathrm{d}\boldsymbol{x}(s_m, \theta_{(r,e)}) = Q(s_m, \theta_{(r,e)})\mathrm{d}\gamma. \tag{68}$$

The Jacobian J on the point m along the ray initialised by the angle $\theta_{(r,e)}$ then satisfies

$$J(s_m, \theta_{(r,e)}) = \det\, Q(s_m, \theta_{(r,e)}), \tag{69}$$

where det denotes the determinant. This ray Jacobian is closely connected to the density of the ray field, which is described by the cross section area of ray tube. Here, the ray tube for the ray $\theta_{(r,e)}$ is defined as a family of rays with an initial angle in the interval $\left(\theta_{(r,e)} - \Delta\theta,\ \theta_{(r,e)} + \Delta\theta\right)$. We can estimate the Jacobian J as the determinant of a matrix which includes the derivative of a ray's trajectory with respect to the ray coordinates using finite differences [34]

$$J\left(s_m, \theta_{(r,e)}\right) = \det\left(\left[\frac{\partial \boldsymbol{x}}{\partial \theta}\left(s_m, \theta_{(r,e)}\right),\ \frac{\partial \boldsymbol{x}}{\partial s}\left(s_m, \theta_{(r,e)}\right)\right]^{\mathrm{T}}\right). \tag{70}$$

The derivative of the ray's trajectory with respect to the arc length s can be approximated using finite differences in the form

$$\frac{\partial \boldsymbol{x}}{\partial s}\left(s_m, \theta_{(r,e)}\right) \approx \frac{\boldsymbol{x}\left(s_{m+1}, \theta_{(r,e)}\right) - \boldsymbol{x}\left(s_{m-1}, \theta_{(r,e)}\right)}{2\Delta s}, \tag{71}$$

where Δs is the user-defined step size used for calculation of the trajectory of the ray (cf section 5). In the same way, the derivative with respect to the polar initial direction can be numerically approximated using

$$\frac{\partial \boldsymbol{x}}{\partial \theta}\left(s_m, \theta_{(r,e)}\right) \approx \frac{\boldsymbol{x}\left(s_m, \theta_{(r,e)} + \Delta\theta\right) - \boldsymbol{x}\left(s_m, \theta_{(r,e)} - \Delta\theta\right)}{2\Delta\theta}, \tag{72}$$

where $\Delta\theta$ is a user-defined perturbation in the initial angle of the linked ray, and is here fixed. The above equation requires tracing two additional auxiliary rays with angles $\theta_{(r,e)} \pm \Delta\theta$ for each emission–reception pair after ray linking [32]. When the reception points are sufficiently close together the computation of auxiliary rays can be avoided by modifying (72) into the form

$$\frac{\partial \boldsymbol{x}}{\partial \theta}\left(s_m, \theta_{(r,e)}\right) \approx \frac{\boldsymbol{x}\left(s_m, \theta_{(r+1,e)}\right) - \boldsymbol{x}\left(s_m, \theta_{(r-1,e)}\right)}{\theta_{(r+1,e)} - \theta_{(r-1,e)}}. \tag{73}$$

Here, $\boldsymbol{x}\left(s_m, \theta_{(r\pm1,e)}\right)$ denotes the position of the two rays linking the emission position $\boldsymbol{x}_e$ to the two nearest reception points $\boldsymbol{x}_{r\pm1}$. (Note that a rotational indexing must be used for the

reception points for a circular detection geometry, i.e. the receivers adjacent to $r = N_r$ are $r = \{N_r - 1, 1\}$.) Using (73), the two auxiliary rays used in (72) are replaced by two adjacent linked rays, which have already been calculated. (Note that (72) is used in this study.) Considering (34), the geometrical attenuation satisfies

$$A_{\text{geom}}\left(\boldsymbol{x}(s_m;\theta_{(r,e)})\right) = \left[\frac{c\left(\boldsymbol{x}(s_m,\theta_{(r,e)})\right)}{c\left(\boldsymbol{x}(s_1,\theta_{(r,e)})\right)}\frac{J(s_1,\theta_{(r,e)})}{J(s_m,\theta_{(r,e)})}\right]^{1/2}, \tag{74}$$

where $J\left(s_1,\theta_{(r,e)}\right)$ is the Jacobian of the ray on the reference point, which is chosen as the second point along the ray, using an assumption that a neighborhood of the emission point with a radius greater than ray spacing Δs is acoustically homogeneous. It is reminded that the acoustic density has been assumed homogeneous in this study.

6.3. Phase

The accumulated phase is discretised in the form

$$\phi\left(\boldsymbol{x}(s_m,\theta_{(r,e)})\right) = \int_{s_0}^{s_m} k\left(\boldsymbol{x}(s_m,\theta_{(r,e)})\right)\mathrm{d}s + \phi\left(\boldsymbol{x}(s_0,\theta_{(r,e)})\right) + \frac{\pi}{2}K(s_m,\theta(r,e)), \tag{75}$$

where $\boldsymbol{x}(s_0,\theta_{(r,e)}) := \boldsymbol{x}_e$ is the emission point. Also, $K(s_m,\theta(r,e))$ is the cumulative times the sign of the ray Jacobian along the ray has been changed. Points on which the ray Jacobian changes sign are called *caustics*, and will lead to a $\pi/2$ shift in the phase [32].

7. Numerical results

This section will describe numerical experiments demonstrating the effectiveness of the proposed ray-based inversion approach for a quantitative reconstruction of the sound speed distribution of an object from the measured pressure time series. In section 7.1, the details for simulation of ultrasound pressure time series are explained. In section 7.2, the Green's function solution to the Szabo's second-order wave equation (12) is compared to a full-wave solution using a *k-space pseudo-spectral* method [35, 46]. This numerical wave solver is freely available in the open-source *k-Wave* toolbox [61, 62]. The reconstructed images will be presented in section 7.3.

7.1. Data simulation

7.1.1. Imaging system and breast phantom. UST data was simulated for an imaging system which consists of 64 emitters and 256 receivers uniformly distributed along a circle with radius $R = 9.5$ cm. A horizontal slice of a 3D digital phantom mimicking the acoustic properties of the breast was used in this study. This digital phantom is freely available [58]. The sound speed was set to a range 1470–1580 m s^{-1}, and the absorption coefficient α_0 was set to a range 0–1 dB MHz^{-y} cm^{-1}, and the power law exponent y was set to 1.4. The sound speed and absorption phantoms are shown in figures 1(a) and (b), respectively. The computational grid consisted of 670×670 grid points with position $[-10.05, +10.02] \times [-10.05, +10.02]\,\text{cm}^2$ and a grid spacing of $\Delta x = 3 \times 10^{-2}$ cm along all the Cartesian coordinates. With this sound speed distribution and grid spacing, the maximum frequency supported by the grid, $f_{\max}$, was 2.45 MHz.

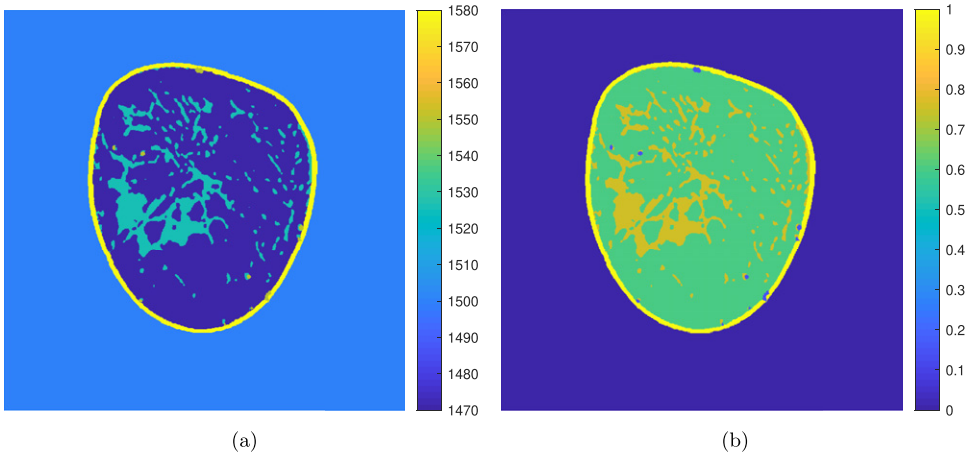

Figure 1. Phantom used for the simulation of the synthetic data using the *k*-wave toolbox: (a) sound speed (m s^{-1}), (b) absorption coefficient (dB MHz^{-y} cm^{-1}), and a homogeneous power law exponent $y = 1.4$.

7.1.2. Simulating time series data. A *k-space pseudo-spectral* method (*k*-wave) was used for simulation of the acoustic pressure time series data [61, 62]. The emitters and receivers were assumed as points (not necessarily lying on grid points), and the interpolation of the pressure field from the grid to these transducers and vice versa was performed using the *off-grid* toolbox [36]. To simulate the data, each emitter was individually driven by an excitation pulse, and the acoustic pressure time series induced at the receivers were recorded simultaneously. This was repeated for each emitter. The pressure time series were recorded at 8621 time points with a sampling rate of 52.8 MHz (18.94 ns time spacing). Additive white Gaussian noise was added to the simulated pressure time series to give a 40 dB signal-to-noise ratio of the peak amplitudes. Two sets of UST data were simulated. The first data set was simulated for only water, and the second data set was simulated for the digital phantom inside water. The computational time for simulation of the UST data set including all excitations for the digital breast phantom inside water using *k*-wave's Matlab code [62] on a single 8-core Xeon E5-2620 v4 2.1 GHz CPU was about 6 h. The output of physical ultrasound transducers covers typically a finite and quite limited bandwidth, and the generated pressure field tends to be more directional at high frequencies. In designing transducers for an imaging system, therefore, a trade-off must be made between the range of frequencies in the excitation pulse and the directionality of the detectors. Although here the transducers are assumed omnidirectional at all frequencies, the frequency bandwidth of the simulated excitation pulse was nevertheless limited. Figure 2(a) shows the normalised amplitude of the excitation pulse (pressure source) in the time domain, and figure 2(b) shows the normalised amplitude and phase components of the excitation pulse in frequency domain, respectively. This signal is used as the pressure source for all excitations. Note that for practical experiments, the induced pressure source may not be the same for different emitters, because it depends on the properties of the emission elements, and a calibration step may be necessary.

7.2. Approximate Green's forward model

In this section, our approximate Green's function solution to Szabo's wave equation (12), proposed in section 3, is compared to a full-wave solution using *k*-wave [46, 61, 62]. Note that

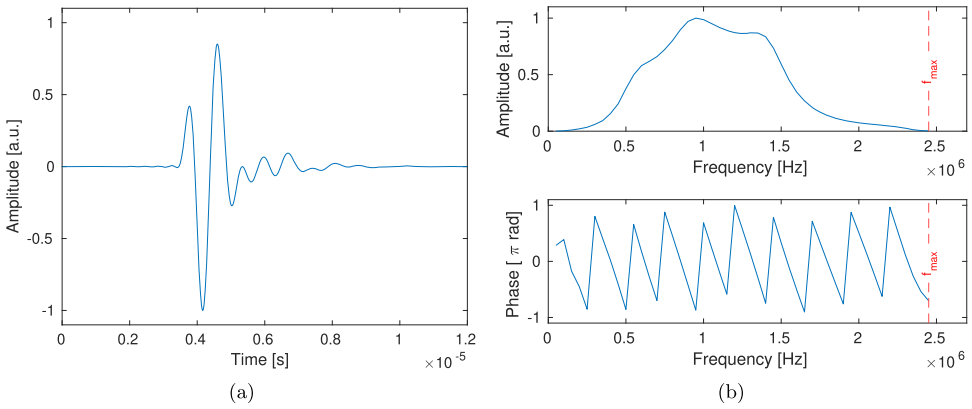

Figure 2. Excitation pulse used for all emitters: (a) time domain, (b) frequency domain: normalised amplitude and phase. $f_{\max}$ indicates the maximum frequency supported by the grid used in the *k*-wave simulations.

k-wave replaces the fractional time derivative in (12) with two fractional Laplacian operators to improve the computational efficiency [46].

7.2.1. Homogeneous medium. The pressure $p(\omega, \boldsymbol{x}; \boldsymbol{x}_e)$ was computed using (16), in which the pressure source was simulated as in figure 2(b), and the Green's function was calculated analytically using the formula (17). The computation was done at 50 equidistant discretised frequencies $\omega \in 0, \ldots, 2\pi f_{\max}$, where $f_{\max}$ is the maximum frequency supported by the computational grid for the *k*-wave simulation. Figures 3(a) and (b) show the amplitude and phase components of the pressure signal measured by receiver 100 after propagation from emitter 1 through water (no breast phantom). The relative discrepancy between the *k*-wave and the ray-based Green's approach for the displayed signal was 0.75%. For the pressure field produced by emitter 1, the mean relative discrepancy between the *k*-wave and Green's approach among the signals recorded by all the 256 receivers was 0.77%. The major portion of the discrepancy corresponds to the interpolation from the emission points to the grid points, and the interpolation from the grid points to the reception points.

7.2.2. Heterogeneous medium. This section compares the forward model using our approximate Green's function approach and *k*-wave for the case of heterogeneous media. The pressure field $p(\omega, \boldsymbol{x}; \boldsymbol{x}_e)$ induced by each emitter, and propagated through the digital breast phantom, was recorded by all 256 receivers. The simulation for *k*-wave was performed as explained above. The pressure field was also approximated using (16), in which the Green's function $g(\omega, \boldsymbol{x}; \boldsymbol{x}_e)$ is approximated using (65) along the linked rays, as described in section 6.

We first compare the *k*-wave solver with the approximate Green's function approach for simulating the pressure field on the receivers. For comparison, *k*-wave was used to simulate the pressure field on the receivers, as described above, and the forward model using the Green's function approach was implemented on the same computational grid and with the same parameters as used for image reconstruction. In the image reconstruction below, the inverse crime was avoided by using two inherently different approaches for the data simulation and image reconstruction steps on different grids. This grid has a size 200×200 with a grid spacing of 1 mm. For implementing the Green's approach, the wave number field has been smoothed by

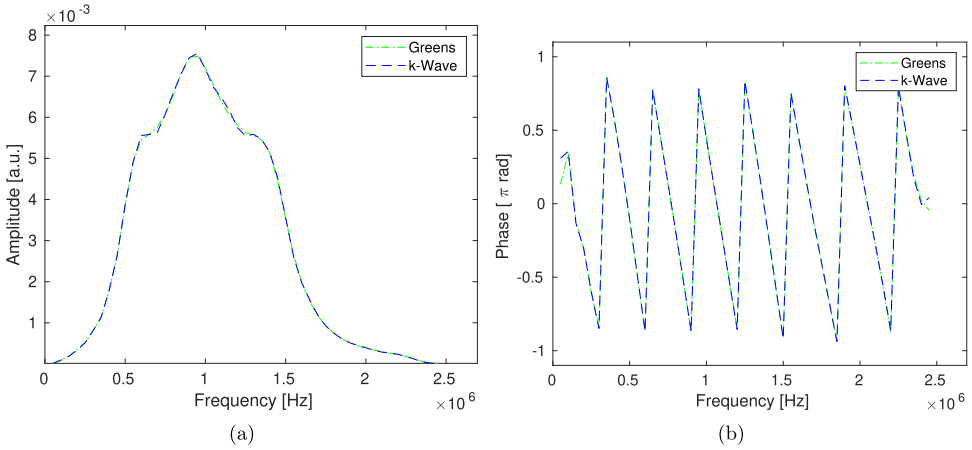

Figure 3. Frequency domain (a) amplitude and (b) phase of the pressure signal measured by receiver 100 after being produced by emitter 1 and propagating through water. (Note that the amplitude has the same normalisation as the excitation signal shown in figure 2(b).).

an averaging window of size 7 grid spacings. Only in this section, for making the comparison fair, the wave number field of the digital breast phantom used for data simulation was smoothed by an equivalent averaging window with size increasing reciprocal of the grid spacing as well. (Note that for simulating the data used for image reconstruction, the *k*-wave was applied on the unsmoothed digital breast phantom.) The reason was that the approximate Green's forward model neglects the scattering effects, but the primary scattering effects will be included in the inversion process as described above.

For both comparison of forward models and image reconstruction, the step size Δs for ray tracing was chosen the same as grid spacing. The ray linking for 2D UST is equivalent to solving a one-dimensional optimisation problem [25]. The most popular one-dimensional approaches for ray linking in 2D UST are *regula falsi* and *secant* methods. The *regula falsi* approach is more time consuming, but is more robust, and more likely gives a stable solution than the *secant* approach when a good initial guess is not available. On the other hand, *secant* method is faster and is a good choice when the initial guess is sufficiently close to the true solution. Only in this section, because ray linking was applied on the digital breast phantom for the purpose of comparison with *k*-wave, a good initial guess is not available. Therefore, *regula falsi* approach was used for ray linking for improving the stability [32].

The accumulated phase along the linked rays was computed using (75). Because the rays are linked between emitters and receivers, the receivers match the last point along the rays, and therefore, the pressure can be approximated on the receivers without any interpolation. The changes in the amplitude because of cumulative acoustic absorption and geometrical spreading were computed along the linked rays using (66) and (74), respectively. For the latter, the amplitude on the second point along the ray was calculated using the analytical formula (20), and using an assumption that a neighborhood of each emission point with a radius larger than the ray spacing is acoustically homogeneous. The Jacobian on the rays' points was computed using (72), which required two auxiliary rays for each linked ray (emitter–receiver pair).

Figures 4(a) and (b) show the discrepancy $(\phi - \phi_0)/\omega$ using an exponent power $y = 2$ (used only for the comparison case), which makes the plot independent of frequency.

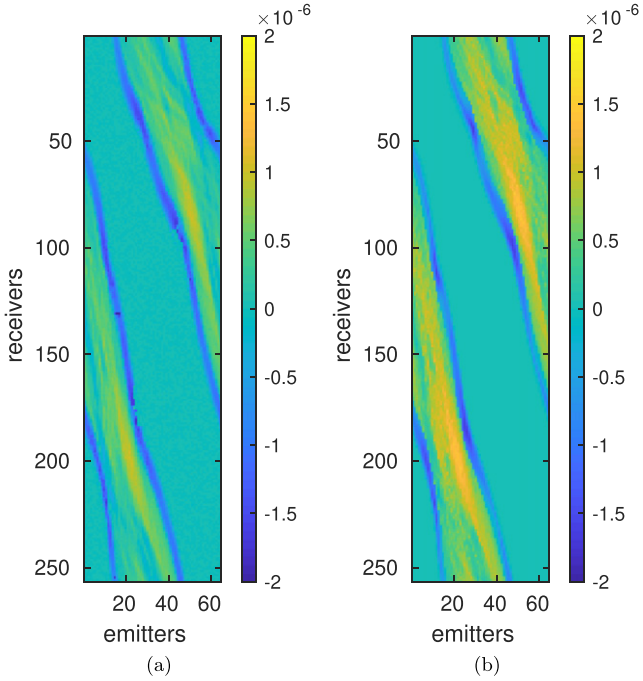

Figure 4. (a) The discrepancy of the TOF of two sets of time traces measured from the pressure field propagating through the breast inside water and only water. The TOFs were computed using a first-arrival picking algorithm [59], and are approximate. (b) Computed $(\phi - \phi_0)/\omega$, which is the same for all frequencies for $y = 2$. Here, ϕ_0 and ϕ are accumulated (unwrapped) phases in water and phantom.

In figure 4(b), ϕ represents the accumulated phase along the linked rays for the digital breast phantom, and was approximated using (75), and ϕ_0 is the phase on the receivers in the only water, and was calculated using (19). An approximate broadband variant of the accumulated (unwrapped) phase of time traces was determined using the TOFs computed using a first-arrival picking algorithm often used for transmission imaging for medical applications [59]. As described, using $y = 2$, the effects of dispersion on the plots are neglected. (Note that for the data simulated for image reconstruction, a more realistic $y = 1.4$ was used.) Figure 4(a) shows the discrepancy of the TOFs in the two sets of time traces measured on the receivers, i.e. propagating in water and the digital breast phantom inside the water. (Recall that the 'measured' signals were simulated using *k*-wave.) In this figure, the columns (resp. rows) represent the emitters (resp. receivers).

Figures 5(a) and (b) compare the *k*-wave and the Green's function approach for the phase component of the pressure field on the receivers at frequency $f = 1$ MHz after being produced by emitters 1 and 33, respectively. Note that in figure 5(a), the rays linking emitter 1 and receivers almost in the ranges smaller than 50 and larger than 200 travel in only water. Also in figure 5(b), the rays linking emitter 33 and receivers roughly in a range 80–180 travel in only water. Therefore, for these rays, the approximate Green's function for only water (equation (17)) and the absorbing breast inside water (equation (65)) give the same pressures, and also the discrepancy with *k*-wave is small, as explained in section 7.2.1. For the rays travelling through the breast, i.e. the rays containing useful information for UST, the *k*-wave and Green's forward model approximated for the absorbing breast give good agreement, but the

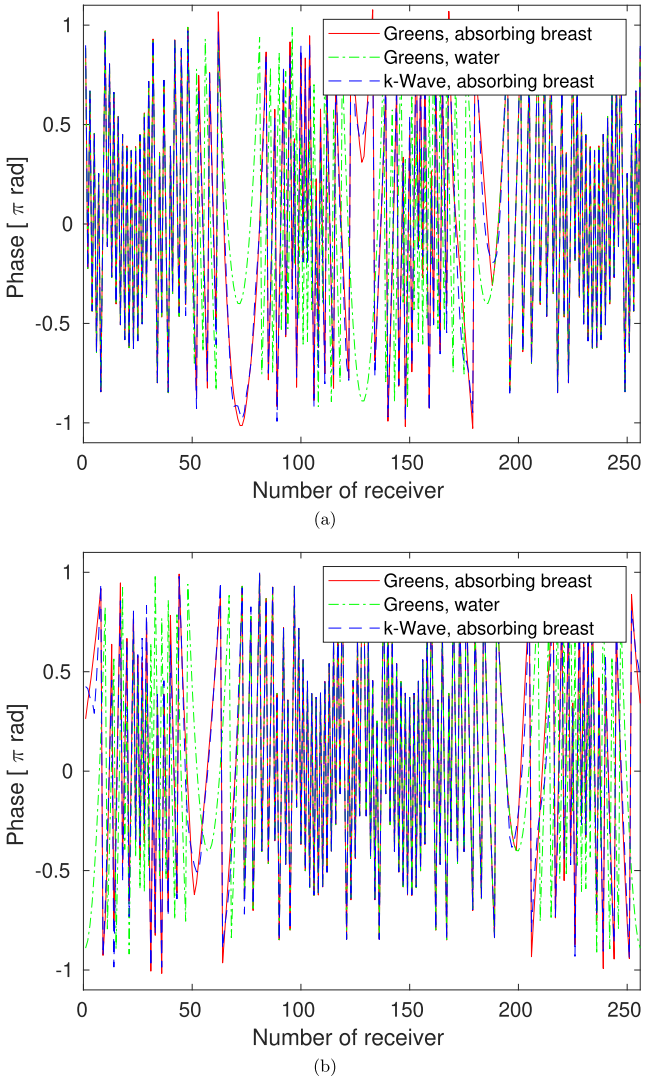

Figure 5. The phase of the pressure field measured on the receivers at $f = 1$ MHz after being produced by: (a) emitter 1 and (b) emitter 33. Approximate Green's forward model with: absorbing breast phantom (red) and water (green), *k*-wave with: absorbing breast (blue).

Green's forward model assuming the only water shows large discrepancies with *k*-wave as expected.

Figures 6(a) and (b) compare the *k*-wave and the Green's approach for the amplitude of the pressure field induced by emitters 1 and 33, and measured on all the receivers at frequency $f = 1$ MHz. Note that in contrast to the approximate Green's forward model, which approximates the amplitude along the linked rays, the *k*-wave simulation also includes the scattering effects, but the smoothing applied on the digital breast phantom (only for comparison purposes), reduces the scattering effects. Note also that for the light blue plot, α_0 is assumed zero, and only the geometrical effects have been accounted for in calculating the amplitudes, i.e.

$A_{\text{abs}} = 1$. It is also reminded that the amplitudes calculated by the analytic Green's function given in (17) (green line) match the amplitudes simulated by k-wave in water, as shown in figure 3(a). Figures 6(a) and (b) show that the amplitudes approximated by the heterogeneous Green's forward model assuming $\alpha_0 = 0$ and the analytical Green's forward model assuming only water have considerable discrepancies with *k*-wave, but the approximate heterogeneous Green's forward model including the acoustic absorption has good agreement with *k*-wave in approximating the amplitudes. The major portion of mismatch between *k*-wave and the heterogeneous Green's forward model includes the scattering effects neglected by the Green's forward model. As explained in section 4, the scattering effects are accounted for in the inverse problem through using a second-order optimisation scheme.

7.3. Image reconstruction

This section gives further details about the procedure used for image reconstruction, and shows the reconstructed images. The grid for image reconstruction consisted of 200×200 grid points with position $[-9.98, +9.93] \times [-9.98, +9.93]\,\text{cm}^2$ and a grid spacing of $\Delta x = 1$ mm along all the Cartesian coordinates. The pressure time series were downsampled by two, providing a sampling rate of 26.4 MHz (37.88 ns time spacing) for the data used for image reconstruction. Because the sound speed is reconstructed on the grid points, the parameters of Green's functions approximated along the linked rays must be interpolated to the grid points. This was done by enforcing a triangulation to the sampled points on the linked rays, and then interpolating the approximated parameters on the rays' points to the grid points using a trilinear interpolation. For computing the Green's function $g(c; \boldsymbol{x}_r; \boldsymbol{x})$, the parameters are reversed along the linked rays. This is equivalent to replacing e and r in formulae given in section 6. Note that for computing the geometrical portion of the amplitude along each reversed ray using equation (72), two additional auxiliary rays must be computed with initial positions $\boldsymbol{x}_r$. The accuracy of the reconstructed images are measured in terms of *relative error*

$$\text{RE}\left(c_{\text{image}}\right) = \frac{\left\|c_{\text{image}} - c_{\text{phantom}}\right\|}{\left\|c_0 - c_{\text{phantom}}\right\|} \times 100, \tag{76}$$

where c_{image} denotes the reconstructed sound speed distribution, and c_0 is the sound speed in water. This parameter is calculated on the grid, and inside the binary mask, used for image reconstruction.

7.3.1. Initial guess. Because the inverse problem of reconstructing the sound speed image from boundary pressure data is nonlinear [49], an initial guess using a TOF approach is often used [18, 19, 50–53, 64]. Here, an image reconstruction approach based on the TOF of the measured pressure data [27, 59] was used in order to provide an initial guess for the proposed inversion approach, but a rough initial guess was chosen using only the early iterations of the TOF-based inversion in order to show that the success of the proposed ray-based Green's inversion approach is not strongly dependent on the image provided by the TOF-based inversion approach.

The discrepancy of the first-arrival of the measured (simulated) pressure time series for the two data sets simulated for the breast phantom inside water and only water was calculated using a first-arrival picking algorithm [59]. The TOF-based inversion approach iteratively minimises the norm of discrepancy of first-arrivals modelled by the ray tracing algorithm 2 and those calculated from the measured data sets using the first-arrival picking algorithm [59]. The sound speed distribution was initialised from the sound speed in water, and the TOFs are iteratively modelled as the integral of the slowness (reciprocal of sound speed) along the linked rays. At

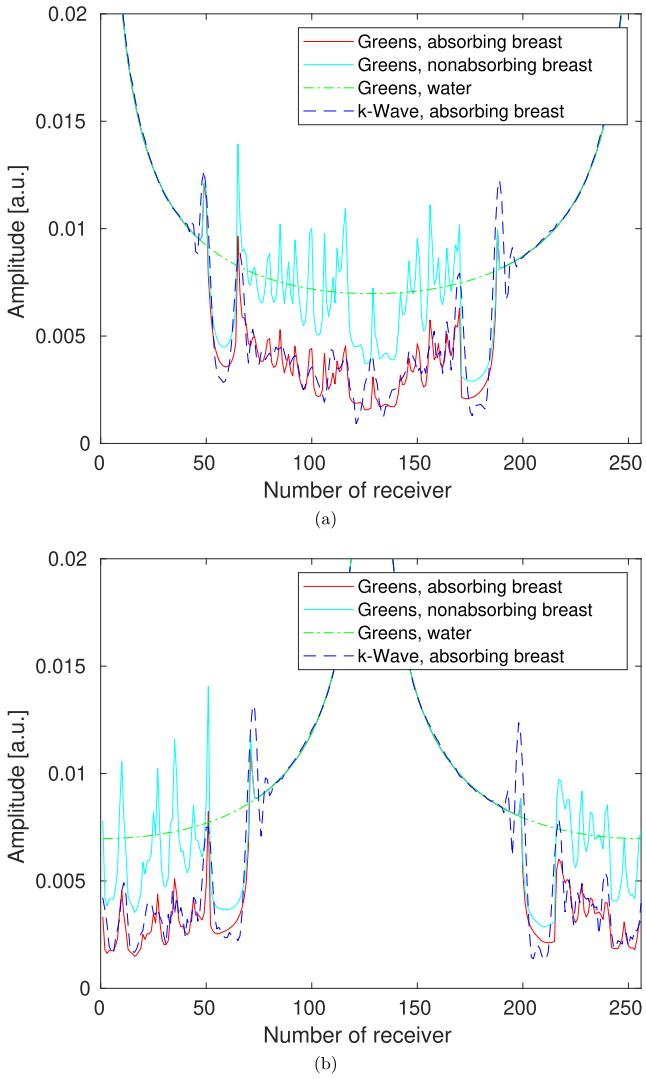

Figure 6. The amplitude of the pressure field measured on the receivers at $f = 1$ MHz after being produced by: (a) emitter 1 and (b) emitter 33. Approximate Green's forward model with: absorbing breast phantom (red), non-absorbing (light blue) and water (green), *k*-wave with: absorbing breast (blue).

each iteration, the ray linking was done separately for all emitter-receiver pairs by an iterative implementation of the ray tracing algorithm 2 using the *secant* method, and the initial angle of each ray (initial guess) for ray linking was chosen as the optimal initial angle obtained from ray linking at the previous iteration [27]. Only for ray tracing associated with the TOF-based inversion approach, the dispersion effects were ignored, i.e. $\alpha = 0$. For ray tracing and construction of the system matrix at each iteration (cf [27]), the sound speed updates were smoothed by an averaging window of size 7 grid spacings. The optimal TOF-based image was obtained after 6 iterations, i.e. one iteration using straight rays following 5 iterations using bent rays applied on the updates of the sound speed map. The first iteration was done using straight rays, because

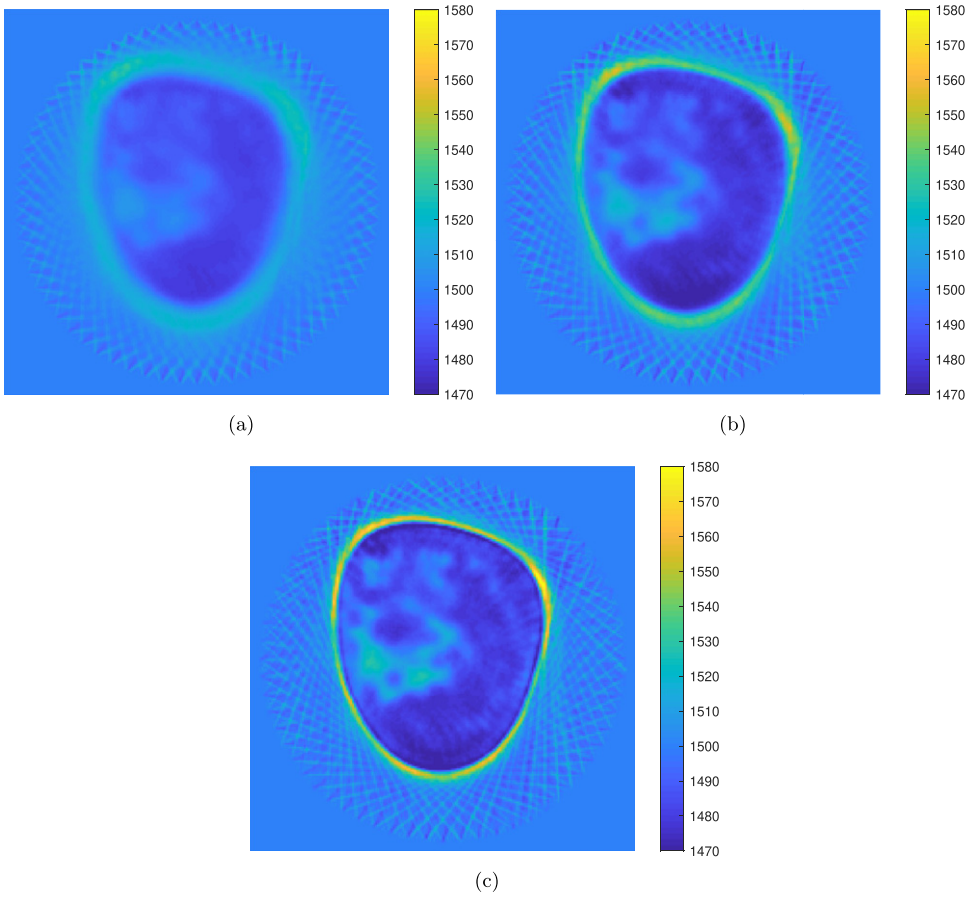

Figure 7. Reconstructed images using TOF data, after: (a) one iteration using straight rays, (b) one iteration using straight rays and 2 iterations using bent rays, (c) one iteration using straight rays and 5 iterations using bent rays (the optimal TOF image).

the initial guess was chosen homogeneous, i.e. the sound speed in water. Figure 7(a) shows the image reconstructed after the first iteration of the TOF-based inversion approach using only straight rays (RE $= 85.09\%$). Figure 7(b) shows the TOF-based reconstructed image after one iteration using straight rays and subsequently 2 iterations using the bent rays (RE $= 75.67\%$). Figure 7(c) shows the optimal image reconstructed by the TOF-based inversion approach after the 6 iterations (RE $= 66.21\%$).

7.3.2. Green's function-based inversion approach. The inversion approach explained in section 4 was implemented at 140 equidistant discretised frequencies $f \in 0.2, \ldots, 1.5$ MHz. The image reconstruction was performed from low to high frequencies such that each linearised subproblem (38) was solved at four consecutive discretised frequencies using algorithm 1. For each linearised subproblem, the Green's functions were approximated along the rays linked in a medium having the last update of the sound speed, computed from the previous linearised subproblem. The ray linking was performed separately for all emitter-receive pairs using the *secant* method. For ray linking, a set of constraints was enforced on the initial angles in order to improve the stability, as explained in [27]. The trajectory of rays are iteratively computed

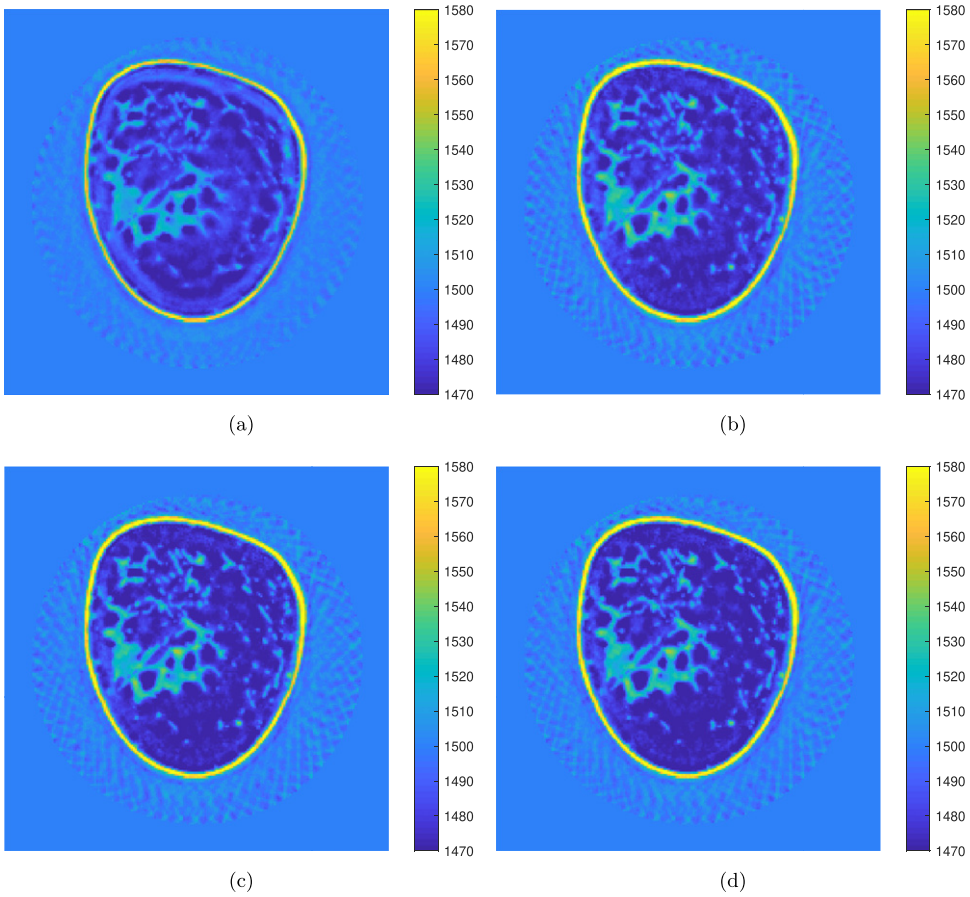

Figure 8. Reconstructed images using the ray-based Green's approach. (a) Using the TOF initial guess shown in figure 7(a), and the true α_0 as shown in figure 1(b). (b) Using the better TOF initial guess shown in figure 7(b), and setting $\alpha_0 = 0$, (c) as (b) but setting $\alpha_0 = 0.5\,\text{dB MHz}^{-y}\,\text{cm}^{-1}$ everywhere, (d) as (b) but with the true α_0.

using algorithm 2 until the end point of the rays matches the position of the reception points within a tolerance [27]. For computing the trajectory of rays, an averaging window of size 7 grid spacings was enforced on the updated wave number fields, but the nonsmoothed updates were used for integration along the rays and approximating the Green's functions using the formulae given in section 6. For each emitter–receiver pair, the initial angle of the linked ray (optimal ray after ray linking) for the linearised subproblem n was used as the initial guess for ray linking for the linearised subproblem $n + 1$ [27]. For $n = 0$, the initial guess for the initial angles were chosen as those obtained from ray linking at the last iteration of the TOF-based inversion approach. Each linearised subproblem was solved using maximum $l_{\max} = 10$ cg iterations (cf algorithm 1).

Figure 8(a) shows the sound speed image reconstructed using the proposed Green's function approach (RE $= 45.98\%$), when the initial guess was chosen to be far from the optimal solution, i.e. the TOF-based sound speed reconstructed using one straight-ray iteration (shown in figure 7(a)), and the true absorption coefficient map shown in figure 1(b) was used for image reconstruction. Figures 8(b)–(d) show the sound speed images reconstructed using the

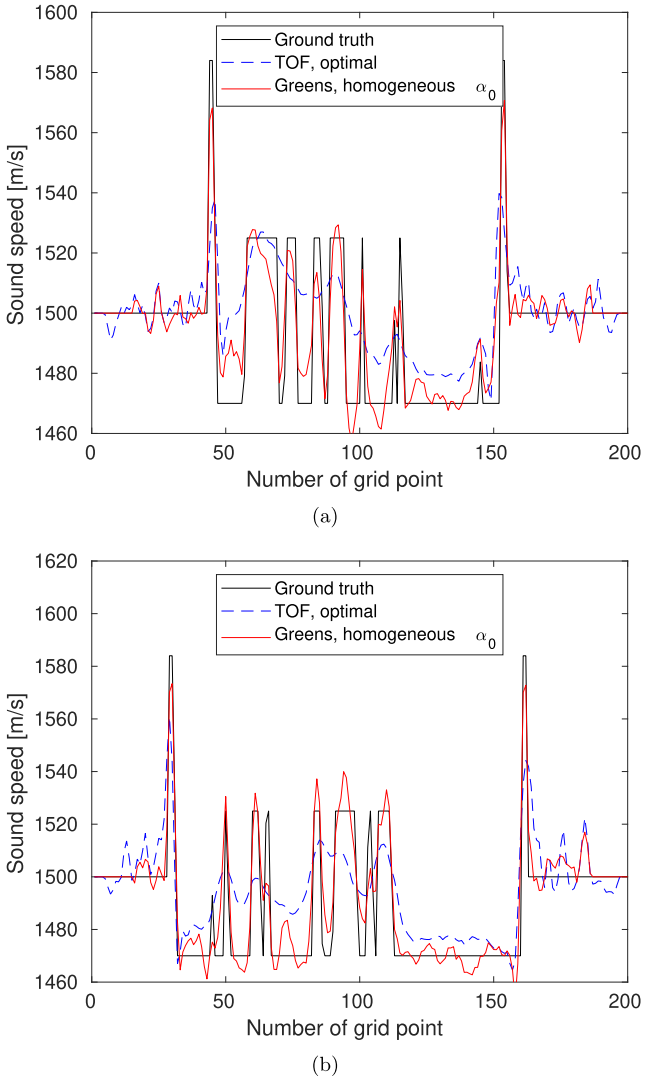

Figure 9. The reconstructed sound speed values for the grid points in the images along: (a) horizontal row ($x = 0$) and (b) vertical column ($y = 0$). The values correspond to the phantom interpolated onto the grid for image reconstruction (black), optimal (best) reconstructed image using the TOF-based approach (blue), and the reconstructed image using the Green's approach assuming a homogeneous absorption coefficient $\alpha_0 = 0.5\,\text{dB MHz}^{-y}\,\text{cm}^{-1}$ across the breast phantom (red).

Green's function approach, when the initial guess was chosen to be the sound speed shown in figure 7(b). Figure 8(b) shows the reconstructed sound speed image (RE $= 42.49\%$), when the absorption and dispersion are neglected by using $\alpha_0 = 0$. Figure 8(c) shows the sound speed image (RE $= 38.95\%$), when the absorption coefficient inside the breast phantom was set homogeneous and $\alpha_0 = 0.5\,\text{dB MHz}^{-y}\,\text{cm}^{-1}$ in order to avoid an inverse crime. Figure 8(d) shows the reconstructed image ($RE = 37.97\%$), when the true absorption coefficient given in figure 1(b) was used. As shown in these images, the discrepancy between the reconstructed

images using the true α_0 and the erroneous homogeneous α_0 is small, but the reconstructed image for which the absorption and dispersion effects are neglected includes more artefact.

Figures 9(a) and (b) provide a clearer comparison between the sound speed values reconstructed by the TOF-based and Green's inversion approaches, as they show profiles of the sound speed along the central row ($x = 0$) and the central column ($y = 0$) in the reconstructed images, respectively. The line plots correspond to the sound speed phantom interpolated onto the grid for image reconstruction (black), the optimal image reconstructed using the TOF-based inversion approach (blue) and the image reconstructed using the Green's inversion approach assuming a homogeneous $\alpha_0 = 0.5\,\text{dB MHz}^{-y}\,\text{cm}^{-1}$ across the breast phantom (red).

It is worth mentioning that for choosing the initial guess of the Green's inversion approach as a sound speed image reconstructed using the TOF-based approach, a trade-off should be made between the closeness to the optimal solution of the Green's approach and the artefact included in the reconstructed image [18, 19].

For purposes of comparison, a reconstruction was performed using only straight rays (not shown). We found that using bent rays resulted in a slightly more accurate sound speed update than using straight rays at low frequencies (200 kHz), but the improvement became greater as the frequency increased.

8. Discussion

In this section we highlight some similarities with other approaches used to tackle UST, and briefly discuss the advantages and disadvantages of this approach compared to other commonly-used approaches. There is a very extensive literature on UST and seismic imaging dating back decades, and, for reasons of space, we cannot reference all possible relevant works here, but we hope those works referenced are representative and give the reader a route into the considerable literature.

Inversions using full-wave models. The most general approach for reconstructing the sound speed from acoustic pressure data is based on minimising the difference (in some sense) between the measurements and a model of the acoustic propagation. This model-based minimisation framework is widely used for tackling inverse problems, and has also been widely used for UST. It is also the approach taken in this paper. Arguably, the choice of model that will achieve the most accurate results is the model that describes the physics of acoustic propagation most accurately. For this reason, there has been great interest recently in using full-wave models that explicitly model the acoustic wave equation for heterogenous media [2, 20, 50–53, 56]. As expected, these approaches have been shown to provide accurate and high resolution images, but a significant hurdle to the practical applicability of these is that the full-wave solvers are compute intensive. Indeed, grid-based solvers become increasingly memory-hungry the higher the frequency. (Another potential disadvantage is when using a rotating measurement system with a sparse distribution of transducers [9, 10], as the number of forward solvers grows linearly with the number of rotations [27].) It is also important to consider that it is never possible to include every conceivable physical effect in any forward model, and that even full-wave models are based on approximations. For example, it is not necessary to model backscattered waves when measurements are only made in front of the emitter. The challenge is balancing the extent to which the physics is modelled accurately with the cost of computation, such that good images can be produced in a reasonable time. For this reason, approximate models have been proposed for use within model-based inversions [17–19]. The approach proposed here falls into this category. Our approximate forward model is based on a ray-approximation to the Green's function for heterogeneous media, and takes into account geometrical spreading (including acoustic refraction), and absorption and dispersion following a frequency power law

evident in tissues, and first-scattered waves. This has two significant advantages over full-wave models: it is much more computationally efficient than grid-based full-wave solvers, and the cost does not scale with frequency. Note that with a grid-based model, the grid spacing must be chosen to support the maximum frequency in the pulse, which is not a limitation in our approach. Bearing this, and the computation time for the full-wave model in mind, we anticipate that our ray-based approach will be about two orders of magnitude faster than a full-wave approach based on such a model for a typical UST system. (cf section 7.1) Also, it is trivial to incorporate any arbitrary transducer element directionality in a ray-based scheme (for transmit and receive), which is less straightforward in full-wave models and can be important in practice. Now, it is well known that ray theory is a very good approximation when the frequency is sufficiently high that it sees the medium as smoothly varying. Here, we showed that this approximation, when embedded in a second-order minimisation scheme, can recover very accurate images for the level of contrast found in soft tissue.

Inversions based on TOF. Ray-based inversion schemes for UST have typically been used when the data is given in the form of a set of TOF between the emitters and receivers. This computationally efficient approach has been widely used in 2D [7, 11–13, 25, 26] and more recently in 3D [27]. In our approach here, we retain the computational efficiency of ray-tracing, but dispense with the drawbacks of TOF picking by using the whole set of acoustic time series in the inversion. TOF picking, by reducing each time series to a single number, removes a great deal of information in the data, effectively reducing the signal-to-noise ratio.

It might be objected that a ray-based forward model, such as that used here and included in the objective function $\mathcal{F}$, does not account for scattering, only refraction, geometric spreading and absorption. While that is true, a key point of our approach is that the Frećhet derivative, included in the Hessian, does take into account the primary scattered waves, so these are included during the image reconstruction (over an increasingly good estimate of the sound speed at each iteration). This is explained in the context of the Born approximation below.

Note that we use ray-tracing to compute the rays, rather than grid-based eikonal solvers [64] such as fast marching, as the latter suffer from similar computational challenges to grid-based full-wave models.

Inversions exploiting the Born-approximation. A common approach to incorporating first-order scattered waves in simulations and inversions is to turn to the Born approximation [16, 22, 48], and in particular the ray-Born approximation [60, 67]. The Born approximation suggests an efficient way for approximating the wavefield using an assumption that the sound speed model can be decomposed into a homogeneous or slowly varying background and a rapidly varying scatterer [68]. It has been studied extensively from both theoretical [65, 66] and numerical points of view [32, 67].

Born forward modelling assumes that the wavefield measured on the receivers consists of two components: the free-space Green's function solution in the homogeneous or slowly varying background medium, and a scattering integral, which accounts for the scattered waves up to the order of a scattering series used for describing the relation between the perturbation in the sound speed and the induced perturbation in the wavefield. This scattering series is referred to as a *Born series* [68]. The first-order approximation of the Born series linearly relates a perturbation to the sound speed to the primarily scattered waves.

The Born approximation was used for including the diffraction of plane waves in the transmission computed tomography [15, 69]. In the context of diffraction tomography, the Fourier diffraction theorem, which relates the Fourier transform of the scattered wavefield to the Fourier transform of the medium's sound speed, can be derived using a first-order Born approximation [70]. In one study, the linearised subproblem derived from a first-order Born approximation about a homogeneous background medium was solved using a filtered

back-projection algorithm, and a delay-and-sum algorithm was used for back-projection of the scattered data [16]. In one clinical application, using a similar approach in frequency domain, it was shown that transmission diffraction tomography relying on the Born approximation provided higher resolution images than TOF-based transmission UST [71]. Recently, iterative optimisation inversion approaches using the Born approximation have received much attention [72–74]. The synthetic data used in these studies were simulated using a similar Born approximation and for simple geometries. In these studies, the heterogeneity of the medium was included in the scattering potential, but the Green's function was fixed, and was defined using the analytic formula (17). However, as shown in figures 5(a) and 6(b), this analytical Green's function can be inaccurate in phase and amplitude for heterogeneous media. In general, the validity of the Born approximation depends on the size (in $L2$ norm sense) of the associated scattering integral. Therefore, the Born approximation using the analytical Greens' function has the drawback that it diverges in the case of a strongly scattering medium [72]. Accordingly, it has been shown that Born approximation using analytical Green's function is valid under certain conditions that may not hold for UST of the breast, i.e. the medium must be weakly scattering, and the object's size must be small sufficiently that the distortion in phase be small [64, 70].

In the context of seismic imaging, the class of ray-based migration/inversion approaches have received much attention [60, 75–77]. Our proposed Born approximation relies on a heterogeneous Green's function for which the distortion in phase and amplitude are accounted for using a novel ray approximation model adapted to UST. The Green's function included in our Born approximation accounts for geometrical spreading including refraction, and physical absorption and dispersion following the frequency power law [43, 44]. (cf section 7.2.2) The scattering effects are accounted for by minimising the objective function using a second-order optimisation scheme. The objective function is minimised separately for a sequence of narrow frequency ranges, each including few number of discretised frequencies, and the minimisation for each frequency range is done by computing a GN step direction, which provides a direct step towards the minimum of the objective function (equation (39)) for that frequency range. For each frequency range, the associated Born approximation provides a linear relation between the scattered waves and the unknown scattering features. From low to high frequencies, the singly scattering features are therefore included in the background medium. This is the first study suggesting such an inversion approach for UST.

Embedding the Born approximation in the introduced optimisation framework using a narrow frequency window moving from low to high frequencies had two advantages. First, the computational cost of computing the inverse of Hessian was significantly reduced, and therefore, including redundant information in the GN step directions was avoided. Second, minimising the objective function from low-to-high frequencies helped ensure the solution did not become stuck in a local minimum. Because of the gradual inclusion of the scatterers in the iteratively-found background medium, the problem of the multivaluedness of the ray field may occur [68]. To tackle this, either more advanced asymptotic modeling techniques such as Gaussian beams should be used [78] at the cost of more computational cost, or the background medium should be smoothed. Here, the latter approach was used such that the rays' trajectory was computed on the sound speed updates that are smoothed by an averaging window. (Note that the smoothed sound speed was used only for calculating rays' trajectory, but phase and amplitudes on the rays were calculated using the nonsmoothed version of the sound speed updates using the formulae in section 6).

Our numerical experience shows that even with enforcing the averaging window on the sound speed (or wavenumber) field, the ray linking is the key step in approximating accurate

pressure time series at the receivers. Avoiding ray linking and tracing the rays using evenly-spaced initial angles, and then interpolating to the reception points will lead to large errors in the approximation of the wavefield at some receivers (not shown). This study established a framework for approximating and discretising heterogeneous Green's function along the linked rays. The linked rays computed for the forward pressure field can also be used for computing the adjoint field.

Absorption. It is evident that the physical absorption and dispersion in soft tissues is frequency dependent, and follows a frequency-power law [44, 45]. This study included these effects by deriving a ray approximation to heterogeneous Green's function relying on Szabo's absorbing wave equation [43, 44]. This study was limited to an image reconstruction of the sound speed given the absorption coefficient map, but it was shown that the proposed method can reconstruct an accurate sound speed map for soft tissues like the breast, when only partial information about the absorption coefficient map is available, i.e. the absorption coefficient map across the breast phantom is assumed homogeneous. The quality of the reconstructed image degrades slightly when the absorption and dispersion effects are fully neglected. It should also be noted that the inversion framework presented here will allow for the extension of this approach to recovering both the absorption and the sound speed simultaneously, because both affect the complex scattering potential $\Upsilon\delta k$.

Practical applicability. Although here, the effectiveness of the proposed inversion approach was demonstrated in a simulation scenario, the inverse crime was avoided by using two inherently different approaches for data simulation and for the forward model in the image reconstruction. Also, the excitation pulse used in this study was the output of a physical transducer, and the number of excitations (emitters) was less than is often used in practice for 2D UST [11], suggesting it will be possible to achieve similar results with experimental data. In addition, the higher-order scattered waves will likely be buried in the noise that is always present in measured UST data, and therefore it is not clear how great the advantage of a full-wave inversion approach will be over our inversion approach.

For nonlinear inverse problems, regularisation is often used for reducing the ill-posedness and improving the stability [51, 53]. Here, although explicit regularisation was avoided, the cg iterations $l_{\max}$ implicitly adjusts the regularisation on the solution, i.e. early stopping of cg iterations in the solution of the linearised subproblems acts as a regulariser.

The proposed approach was proposed and demonstrated for a 2D scenario, but the acoustic waves actually travel in 3D medium. An extension of the proposed approach to 2.5D, i.e. imaging within a slab-like volume containing a target slice along the detection ring [39], or full-3D [9, 10], is straightforward, and will be studied in future work. A key challenge in extending this approach to 3D is 3D ray-linking; we recently proposed an efficient and robust approach to overcome this [27].

9. Summary

An efficient UST image reconstruction algorithm is described and demonstrated for recovering the sound speed distribution from acoustic time series measurements made in soft tissue. The approach is based on a second-order iterative minimisation of the difference between the measurements and a model based on a ray-approximation to the heterogeneous Green's function, and is applied from low to high frequencies.

Acknowledgments

This work was funded by the European Union's Horizon 2020 Research and Innovation Program H2020 ICT 2016–2017 under Grant agreement No. 732411, which is an initiative of the Photonics Public Private Partnership. The authors would like to thank several people for helpful discussions around the topic of this paper. In particular, Marta Batcke and Francesc Rul·lan on rays, Felix Lucka on UST, and Bradley Treeby on *k*-Wave.

Data availability statement

The data that support the findings of this study are available upon reasonable request from the authors.

Appendix A

A.1. Derivation of Hessian matrix

Here, further details will be given about the Hessian matrix (cf equation (52)). Considering (38), the Hessian matrix satisfies

$$H^{(n)}(\boldsymbol{x},\boldsymbol{x}') = \frac{\partial}{\partial c^{(n)}(\boldsymbol{x}')}\left[\frac{\partial \mathcal{F}(c^{(n)})}{\partial\left(c^{(n)}(\boldsymbol{x})\right)}\right] = \frac{\partial}{\partial\left(c^{(n)}(\boldsymbol{x}')\right)}\nabla\mathcal{F}^{(n)}(\boldsymbol{x}). \tag{77}$$

Plugging equation (51) into the right-hand side of the above equation gives two terms [57]

$$H^{(n)}(\boldsymbol{x},\boldsymbol{x}') = H_1^{(n)}(\boldsymbol{x},\boldsymbol{x}') + H_2^{(n)}(\boldsymbol{x},\boldsymbol{x}'), \tag{78}$$

where the first term is in the form

$$H_1^{(n)}(\boldsymbol{x},\boldsymbol{x}') = \sum_{e,r}\int \mathrm{Re}\left\{\frac{\partial}{\partial\left(c^{(n)}(\boldsymbol{x}')\right)}\left[g(c^{(n)};\boldsymbol{x}_r;\boldsymbol{x})\Upsilon_c^{(n)}(\boldsymbol{x})\right.\right.$$
$$\left.\left.\times\left[g(c^{(n)};\boldsymbol{x};\boldsymbol{x}_e)s(\boldsymbol{x}_e)\right]\right]\ \delta p^*_{\mathrm{res}}(c^{(n)};r;e)\right\}\mathrm{d}\omega. \tag{79}$$

Here,

$$\frac{\partial}{\partial\left(c^{(n)}(\boldsymbol{x}')\right)}\left[g(c^{(n)};\boldsymbol{x}_r;\boldsymbol{x})\Upsilon_c^{(n)}(\boldsymbol{x})\left[g(c^{(n)};\boldsymbol{x};\boldsymbol{x}_e)s(\boldsymbol{x}_e)\right]\right]$$
$$= \left(\frac{\partial}{\partial\left(c^{(n)}(\boldsymbol{x}')\right)}\Upsilon_c^{(n)}(\boldsymbol{x})\right)\ g(c^{(n)};\boldsymbol{x}_r;\boldsymbol{x})\left[g(c^{(n)};\boldsymbol{x};\boldsymbol{x}_e)s(\boldsymbol{x}_e)\right]$$
$$+\ \Upsilon_c^{(n)}(\boldsymbol{x})\ \frac{\partial}{\partial\left(c^{(n)}(\boldsymbol{x}')\right)}\left(g(c^{(n)};\boldsymbol{x}_r;\boldsymbol{x})\left[g(c^{(n)};\boldsymbol{x};\boldsymbol{x}_e)s(\boldsymbol{x}_e)\right]\right), \tag{80}$$

where in the last line in the above equation,

$$\frac{\partial}{\partial\left(c^{(n)}(\boldsymbol{x}')\right)}\left(g(c^{(n)};\boldsymbol{x}_r;\boldsymbol{x})\left[g(c^{(n)};\boldsymbol{x};\boldsymbol{x}_e)s(\boldsymbol{x}_e)\right]\right)$$
$$= g(c^{(n)},\boldsymbol{x}_r;\boldsymbol{x}')\Upsilon_c^{(n)}(\boldsymbol{x}')g(c^{(n)},\boldsymbol{x}';\boldsymbol{x})\left[g(c^{(n)};\boldsymbol{x};\boldsymbol{x}_e)s(\boldsymbol{x}_e)\right]$$
$$+ g(c^{(n)},\boldsymbol{x}_r;\boldsymbol{x})g(c^{(n)},\boldsymbol{x};\boldsymbol{x}')\Upsilon_c^{(n)}(\boldsymbol{x}')g(c^{(n)},\boldsymbol{x}';\boldsymbol{x}_e)s(\boldsymbol{x}_e), \tag{81}$$

where the derivatives have been calculated using equation (48).

Also, the second term $H_2^{(n)}$ satisfies

$$H_2^{(n)}(\boldsymbol{x},\boldsymbol{x}') = \sum_{e,r}\int \mathrm{Re}\left\{\left[\Upsilon_c^{(n)}(\boldsymbol{x})\left[g(c^{(n)};\boldsymbol{x};\boldsymbol{x}_e)s(\boldsymbol{x}_e)\right]\right]\right.$$
$$\left.\times\quad\left[g(c^{(n)};\boldsymbol{x}_r;\boldsymbol{x})\frac{\partial p^*_{(c^{(n)};r;e)}}{\partial(c^{(n)}(x'))}\right]\right\}\mathrm{d}\omega, \tag{82}$$

where we have used $\partial/\partial\left(c^{(n)}(\boldsymbol{x}')\right)\left(p_{(c^{(n)};r;e)}\right) = \partial/\partial\left(c^{(n)}(\boldsymbol{x}')\right)\left(\delta p_{\mathrm{res}}(c^{(n)};r;e)\right)$.

Considering that the terms in $H_1^{(n)}$ is negligible compared to the second term $H_2^{(n)}$, and also using the reciprocity of Green's function $g(c^{(n)};\boldsymbol{x}_r;\boldsymbol{x})$, gives a very good approximation to the action of the Hessian on the sound speed perturbation, as given in (52).

A.2. Greens function for 3D case

In the 3D case the homogeneous, lossless Green's function is

$$g_{0,3\mathrm{D}}(\omega,\boldsymbol{x};\boldsymbol{x}') = A_0(\boldsymbol{x};\boldsymbol{x}')\exp\left(\mathrm{i}\phi_0(\boldsymbol{x};\boldsymbol{x}')\right), \tag{83}$$

where $\phi_0 = k_0|\boldsymbol{x}-\boldsymbol{x}'|$ as for the 2D case but there is spherical rather than cylindrical spreading:

$$A_0(\boldsymbol{x};\boldsymbol{x}') = (4\pi|\boldsymbol{x}-\boldsymbol{x}'|)^{-1} = k_0(4\pi\phi_0(\boldsymbol{x},\boldsymbol{x}'))^{-1}. \tag{84}$$

So the approximate Green's function for the heterogeneous, absorbing case can be written by analogy as

$$g_{3\mathrm{D}}(\omega,\boldsymbol{x};\boldsymbol{x}') = A(\boldsymbol{x};\boldsymbol{x}')\exp\left(\mathrm{i}\phi(\boldsymbol{x};\boldsymbol{x}')\right). \tag{85}$$

ORCID iDs

Ashkan Javaherian https://orcid.org/0000-0003-0798-3196
Ben Cox https://orcid.org/0000-0001-7296-4093

References

[1] Tromp J 2020 Seismic wavefield imaging of Earth's interior across scales *Nat. Rev. Earth Environ.* **1** 40–53
[2] Lucka F, Pérez-Liva M, Treeby B and Cox B 2021 High resolution 3D ultrasonic breast imaging by time-domain full waveform inversion (arXiv:2102.00755)
[3] Rullan F and Betcke M 2018 Hamilton–Green solver for the forward and adjoint problems in photoacoustic tomography (arXiv:1810.13196)

[4] Rullan F 2020 Photoacoustic tomography: flexible acoustic solvers based on geometrical optics *PhD Thesis* University College London
[5] Beck A 2017 *First-order Methods in Optimization* (Philadelphia, PA: SIAM)
[6] Hopp T, Ruiter N, Bamber J C, Duric N and van Dongen K W A (ed) 2017 *International Workshop on Medical Ultrasound Tomography* (Germany: Speyer)
[7] Greenleaf J F, Johnson S A, Lee S L, Hermant G T and Woo E H 1974 Algebraic reconstruction of spatial distributions of acoustic absorption within tissue from their two-dimensional acoustic projections *Acoustical Holography* ed P S Green pp 591–603
[8] Opielinski K J, Pruchnicki P, Szymanowski P, Szepieniec W K, Szweda H, Swis E, Jozwik M, Tenderenda M and Bułkowskif M 2018 Multimodal ultrasound computer-assisted tomography: an approach to the recognition of breast lesions *Comput. Med. Imag. Graph.* **65** 102–14
[9] Ruiter N V, Zapf M, Hopp T, Dapp R, Kretzek E, Birk M, Kohout B and Gemmeke H 2012 3D ultrasound computer tomography of the breast: a new era? *Eur. J. Radiol.* **81** S133–4
[10] Gemmeke H, Hopp T, Zapf M, Kaiser C and Ruiter N V 2017 3D ultrasound computer tomography: hardware setup, reconstruction methods and first clinical results *Nucl. Instrum. Methods Phys. Res. Sect. A Accel. Spectrom. Detect. Assoc. Equip.* **873** 59–65
[11] Duric N, Littrup P, Poulo L, Babkin A, Pevzner R, Holsapple E, Rama O and Glide C 2007 Detection of breast cancer with ultrasound tomography: first results with the computed ultrasound risk evaluation (CURE) prototype *Med. Phys.* **34** 773–85
[12] Li C, Duric N, Littrup P and Huang L 2009 *In vivo* breast sound-speed imaging with ultrasound tomography *Ultrasound Med. Biol.* **35** 1615–28
[13] Anderson A H and Kak A C 1984 Simultaneous algebraic reconstruction techniques (SART): a superior implementation of the ART algorithm *Ultrason. Imaging* **6** 81–94
[14] Johnson S A, Greenleaf J F, Samayoa W F, Duck F A and Sjostrand J 1975 Reconstruction of three-dimensional velocity fields and other parameters by acoustic ray tracing *IEEE Proc. Ultrasonics Sympos.* pp 46–51
[15] Devaney A J and Oristaglio M L 1983 Inversion procedure for inverse scattering within the distorted-wave Born approximation *Phys. Rev. Lett.* **51** 237–40
[16] Douglas Mast T 2002 Aberration correction for time-domain ultrasound diffraction tomography *J. Acoust. Soc. Am.* **112** 55–64
[17] Borup D T, Johnson S A, Kimz W W and Berggren M J 1992 Nonperturbative diffraction tomography via Gauss–Newton iteration applied to the scattering integral equation *Ultrason. Imaging* **14** 69–85
[18] Wiskin J, Borup D T, Johnson S A and Berggren M 2012 Non-linear inverse scattering: high resolution quantitative breast tissue tomography *J. Acoust. Soc. Am.* **131** 3802–13
[19] Wiskin J W, Borup D T, Iuanow E, Klock J and Lenox M W 2017 3D nonlinear acoustic inverse scattering: algorithm and quantitative results *IEEE Trans. Ultrason. Ferroelectr. Freq. Control* **64** 1161–74
[20] Goncharsky A V and Romanov S Y 2017 Iterative methods for solving coefficient inverse problems of wave tomography in models with attenuation *Inverse Problems* **33** 025003
[21] Beydoun W B and Tarantola A 1988 First Born and Rytov approximations: modeling and inversion conditions in a canonical example *J. Acoust. Soc. Am.* **83** 1045–55
[22] Engquist B and Runborg O 2003 Computational high frequency wave propagation *Acta Numer.* **12** 181–266
[23] Chapman C 2004 *Fundamentals of Seismic Wave Propagation* (Cambridge: Cambridge University Press)
[24] Runborg O 2007 Mathematical models and numerical methods for high frequency waves *Commun. Comput. Phys.* **2** 827–80
[25] Anderson A H and Kak A C 1982 Digital ray tracing in two-dimensional refractive fields *J. Acoust. Soc. Am.* **72** 1593–606
[26] Anderson A H 1990 A ray tracing approach to restoration and resolution enhancement in experimental ultrasound tomography *Ultrason. Imaging* **12** 268–91
[27] Javaherian A, Lucka F and Cox B T 2020 Refraction-corrected ray-based inversion for three-dimensional ultrasound tomography of the breast *Inverse Problems* **36** 125010
[28] Bold G E J and Birdsall T G 1986 A top-down philosophy for accurate numerical ray tracing *J. Acoust. Soc. Am.* **80** 656–60
[29] Kreyszig E 1993 *Advanced Engineering Mathematics* (New York: Wiley)

[30] Virieux J and Farra V 1991 Ray tracing in 3D complex isotropic media: an analysis of the problem *Geophysics* **56** 2057–69
[31] Denis F, Basset O and Giminez G 1995 Ultrasonic transmission tomography in refracting media: reduction of refraction artefacts by curved-ray techniques *IEEE Trans. Med. Imag.* **14** 173–88
[32] Červený V 2001 *Seismic Ray Theory* (Cambridge: Cambridge University Press)
[33] Butcher J C 1987 *The Numerical Analysis of Ordinary Differential Equations* (*Runge–Kutta and General Linear Methods*) (New York: Wiley)
[34] Holm D 2011 *Geometric Mechanics* (*Part 1: Dynamics & Symmetry*) (London: Imperial College Press) 2nd edn pp 1–97
[35] Cox B T, Kara S, Arridge S R and Beard P C 2007 *k*-space propagation models for acoustically heterogeneous media: application to biomedical photoacoustics *J. Acoust. Soc. Am.* **121** 3453
[36] Wise E S, Cox B T, Jaros J and Treeby B E 2019 Representing arbitrary acoustic source and sensor distributions in Fourier collocation methods *J. Acoust. Soc. Am.* **146** 278–88
[37] Abramowitz M and Stegun I A 1972 *Handbook of Mathematical Functions* 10th edn (New York: Dover Publications, Inc.)
[38] Ali R, Hsieh S and Dahl J 2019 Open-source Gauss–Newton-based methods for refraction-corrected ultrasound computed tomography *Proc. SPIE 10955, Medical Imaging 2019: Ultrasonic Imaging and Tomography, 1095508*
[39] Li S, Jackowski M, Dione D P, Varslot T, Staib L H and Mueller K 2010 Refraction corrected transmission ultrasound computed tomography for application in the breast imaging *Med. Phys.* **37** 2233–46
[40] Rawlinson N, Houseman G A and Collins C D N 2001 Inversion of seismic refraction and wide-angle reflection traveltimes for three-dimensional layered crustal structure *Geophys. J. Int.* **145** 381–400
[41] Rawlinson N, Hauser J and Sambridge M 2008 Seismic ray tracing and wavefront tracking in laterally heterogeneous media *Adv. Geophys.* **49** 203–73
[42] Liebler M, Ginter S, Dreyer T and Riedlinger R E 2004 Full wave modeling of therapeutic ultrasound: efficient time-domain implementation of the frequency power-law attenuation *J. Acoust. Soc. Am.* **116** 2742–50
[43] Szabo T L 1994 Time domain wave equations for lossy media obeying a frequency power law *J. Acoust. Soc. Am.* **96** 491–500
[44] Kelly J F, McGough R J and Meerschaert M M 2008 Analytical time-domain Green's functions for power-law media *J. Acoust. Soc. Am.* **124** 2861–72
[45] Treeby B E and Cox B T 2010 Modeling power law absorption and dispersion for acoustic propagation using the fractional Laplacian *J. Acoust. Soc. Am.* **127** 2741–8
[46] Treeby B E, Zhang E Z and Cox B T 2010 Photoacoustic tomography in absorbing acoustic media using time reversal *Inverse Problems* **26** 115003
[47] Goncharsky A V and Romanov S Y 2014 Inverse problems of ultrasound tomography in models with attenuation *Phys. Med. Biol.* **59** 1979–2004
[48] Mojabi P and LoVetri J 2015 Ultrasound tomography for simultaneous reconstruction of acoustic density, attenuation, and compressibility profiles *J. Acoust. Soc. Am.* **137** 1813–25
[49] Plessix R-E 2006 A review of the adjoint-state method for computing the gradient of a functional with geophysical applications *Geophys. J. Int.* **167** 495–503
[50] Wang K, Matthews T, Anis F, Li C, Duric N and Anastasio M A 2015 Waveform inversion with source encoding for breast sound speed reconstruction in ultrasound computed tomography *IEEE Trans. Ultrason. Ferroelectr. Freq. Control* **62** 475–93
[51] Matthews T P, Wang K, Li C, Duric N and Anastasio M A 2017 Regularized dual averaging image reconstruction for full-wave ultrasound computed tomography *IEEE Trans. Ultrason. Ferroelectr. Freq. Control* **64** 811–25
[52] Matthews T P and Anastasio M A 2017 Joint reconstruction of the initial pressure and speed of sound distributions from combined photoacoustic and ultrasound tomography measurements *Inverse Problems* **33** 124002
[53] Pérez-Liva M, Herraiz J L, Udías J M, Miller E, Cox B T and Treeby B E 2017 Time domain reconstruction of sound speed and attenuation in ultrasound computed tomography using full wave inversion *J. Acoust. Soc. Am.* **141** 1595–604
[54] Guasch L, Calderón Agudo O, Tang M-X, Nachev P and Warner M 2020 Full-waveform inversion imaging of the human brain *npj Digit. Med.* **3** 28

[55] Barnett A and Greengard L 2011 A new integral representation for quasi-periodic scattering problems in two dimensions *BIT Numer. Math.* **51** 67–90
[56] Bachmann E and Tromp J 2020 Source encoding for viscoacoustic ultrasound computed tomography *J. Acoust. Soc. Am.* **147** 3221–35
[57] Margrave G, Yedlin M and Innanen K 2011 Full waveform inversion and the inverse Hessian *CREWES Research Report* **vol 23** 1–13
[58] Lou Y, Zhou W, Matthews T P, Appleton C M and Anastasio M A 2017 Generation of anatomically realistic numerical phantoms for photoacoustic and ultrasonic breast imaging *J. Biomed. Opt.* **22** 041015
[59] Li C, Huang L, Duric N, Zhang H and Rowe C 2009 An improved automatic time-of-flight picker for medical ultrasound tomography *Ultrasonics* **49** 61–72
[60] Coates R T and Chapman C H 1990 Ray perturbation theory and the Born approximation *Geophys. J. Int.* **100** 379–92
[61] Treeby B E and Cox B T 2010 *k*-wave: MATLAB toolbox for the simulation and reconstruction of photoacoustic wave fields *J. Biomed. Opt.* **15** 021314
[62] Treeby B, Cox B and Jaros J *k-Wave: A Matlab Toolbox for the time-domain simulation of acoustic waves* www.k-Wave.org
[63] Pierce A D 1981 *Acoustics An Introduction to its Physical Principles and Applications* 3rd edn (MA: ASA Press)
[64] Huthwaite P and Simonetti F 2011 High-resolution imaging without iteration: a fast and robust method for breast ultrasound tomography *J. Acoust. Soc. Am.* **130** 1721–34
[65] Hudson J A 1977 Scattered waves in the coda of P *J. Geophys.* **43** 359–74
[66] Hudson J A and Heritage J R 1981 The use of the Born approximation in seismic scattering problems *Geophys. J. Int.* **66** 221–40
[67] Sarajaervi M and Keers H 2018 Computation of ray-Born seismograms using isochrons *Geophysics* **83** T245–56
[68] Moser T J 2012 Review of ray-Born forward modeling for migration and diffraction analysis *Stud. Geophys. Geod.* **56** 411–32
[69] Devaney A J 1982 A filtered backpropagation algorithm for diffraction tomography *Ultrason. Imaging* **4** 336–50
[70] Kak C and Slaney M 1998 *Principles of Computerized Tomographic Reconstruction* (Piscataway, NJ: IEEE) pp 203–18
[71] Simonetti F, Huang L, Duric N and Littrup P 2009 Diffraction and coherence in breast ultrasound tomography: a study with a toroidal array *Med. Phys.* **36** 2955
[72] Yun X, He J, Carevic A, Slapnicar I, Barlow J and Almekkawy M 2018 Reconstruction of ultrasound tomography for cancer detection using total least squares and conjugate gradient method *Proc. SPIE 10580, Medical Imaging 2018: Ultrasonic Imaging and Tomography, 105800K*
[73] Carevic , Yun X, Lee G, Slapnicar I, Abdou A, Barlow J and Almekkawy M 2018 Solving the ultrasound inverse scattering problem of inhomogeneous media using different approaches of total least squares algorithms *Proc. SPIE 10580, Medical Imaging 2018: Ultrasonic Imaging and Tomography, 105800J*
[74] Carevic X Y and Almekkawy M 2019 Adaptive truncated total least square on distorted born iterative method in ultrasound inverse scattering problem *Proc. SPIE 10955, Medical Imaging 2019: Ultrasonic Imaging and Tomography, 1095515*
[75] Thierry P, Operto S and Lambaré G 1999 Fast 2D ray+Born migration/inversion in complex media *Geophysics* **64** 162–81
[76] Lambaré G, Virieux J, Madariaga R and Jin S 1992 Iterative asymptotic inversion in the acoustic approximation *Geophysics* **57** 1138–54
[77] Lambare G, Operto S, Podvin P and Thierry P 2003 3D ray+Born migration/inversion: Part 1. Theory *Geophysics* **68** 1348–56
[78] Cerveny V and Pšenčik I Gaussian beams and paraxial ray approximation in three-dimensional elastic inhomogeneous media *J. Geophys.* 53 1–15